

VALUE-ADDED PRODUCTS FROM THE ENLARGED WOMBAT REACTOR.

David L. Wertz, Stephen B. DuBose, Sheila Kosbab, Ashley D. Trahan, Johanna Wolf, Callie Bounds, and E. Ryan Smith, Department of Chemistry & Biochemistry and the Honors College, University of Southern Mississippi, Hattiesburg, MS 39406.

Key words: degrading tires, value-added products.

The WOMBAT process has been utilized to degrade scrap tires into several materials -- a black powder, a mat which has a shape similar to that of the original tire, fibers, steel, and highly discolored nitric acid.¹ Each of these materials is produced in large quantities, and the utilization of each is necessary to produce an environmentally acceptable and an economically useful bottom line for this method. The WOMBAT process has the potential for high through put of tires, and the tires do not require any pre-treatment. After the steel belts have been cleaved from the styrene-butadiene (SBR) matrix of the tire, the belts may be recovered from the reactor with minimal surface corrosion. Both the black powder and the SBR mats may be separated from the fibers and from each other. A schematic of the new and enlarged WOMBAT reactor is presented in Figure 1.

The chemistry of the WOMBAT process may be traced, to some extent, using x-ray fluorescence (XRF) spectrometry. The XRF experiment measures the secondary Xrays emitted by a sample using a separation technique based either on the differences in energies of the emitted Xrays or their differences in wavelengths.² For these experiments, a rhodium x-ray tube (operating at 35 kV and 30 ma) and a graphite monochromator were used. Shown in Figure 2 is the WDXRF spectrum of a 1" x 1" x 1/4" piece of a tire. This spectrum contains several orders of the K_{β} and K_{α} wavelengths emitted by zinc (normally present in the 2-3% range in tires) which occur at $\lambda = 1.30 \text{ \AA}$ and $\lambda = 1.44 \text{ \AA}$, respectively. Also noted is the K_{α} wavelength for sulfur (normally present in the 1.0-2.0% range in tires) at 5.37 \AA . Shown in Figure 3 is the WDXRF spectrum of the black powder recovered from the WOMBAT process. There is no K_{β} and K_{α} peaks indicative of zinc in this spectrum, indicating that the abundance of zinc in the black powder < the lower limit of detection for zinc in this sample. However, the sulfur K_{α} peak, at $\lambda = 5.37 \text{ \AA}$, is clearly discernible in this WDXRF spectrum, indicating that sulfur is retained in this powder.

In previous experiments, it has been shown that the black powder has an energy content ca. 30% higher than the typical bituminous coal and produces <1% high temperature ash. It may be co-combusted with lower energy fuels such as lignite and/or sawdust. However, because the powder retains sulfur, it may be used in processes that require vulcanized materials. Furthermore, because of its high surface area/mass ratio, the black powder also has potential for sequestering metal ions. Shown in Figure 4 is the WDXRF spectra of (a) the black powder and (b) the black powder after it had been dispersed into a solution containing copper(II) nitrate and then recovered. The latter spectrum contains large K_{β} and K_{α} x-ray peaks (at $\lambda = 1.39 \text{ \AA}$ and $\lambda = 1.54 \text{ \AA}$, respectively) due to copper. Subsequent experiments have shown that most of the copper(II) sequestered onto the black powder may be removed from the powder by washing with water.

Having shown that the black WOMBAT powder will sequester copper(II) from an aqueous solution, we are investigating the sequestration properties of the powder towards other metal ions present in water, soil, and air and are also investigating its capabilities for sequestering organic moieties.

The SBR matrix, the other high carbon material recovered from the degradation of the tire, may be cleanly separated from the tire's steel belts and fibers. This SBR matrix, whose WDXRF spectrum is presented in Figure 5, contains considerable amounts of zinc, iron, and sulfur -- as evidenced by the characteristic peaks for these elements in the resulting WDXRF spectrum. This matrix has a high fuel value and produces only 3-4% HTA. In addition, as shown in the x-ray diffractogram presented in Figure 6, the HTA is principally ZnO.

The discolored WOMBAT liquid, which has a considerably reduced oxidizing powder, may be converted to inorganic nitrate salts such as potassium nitrate or ammonium nitrate. The x-ray diffractogram of the chemical product produced when the used WOMBAT liquid is reacted with potassium hydroxide is presented in Figure 7.

REFERENCES.

1. Wertz, D. L. et al., *Am. Chem. Soc., Div. Fuel Chem.*, 1998, 43, 796; 1998, 43, 349; 1997, 42, 741; 1995, 40, 879; 1994, 39, 815.
2. Jenkins, R., "X-Ray Fluorescence Spectrometry"; John Wiley & Sons, NY, 1988.

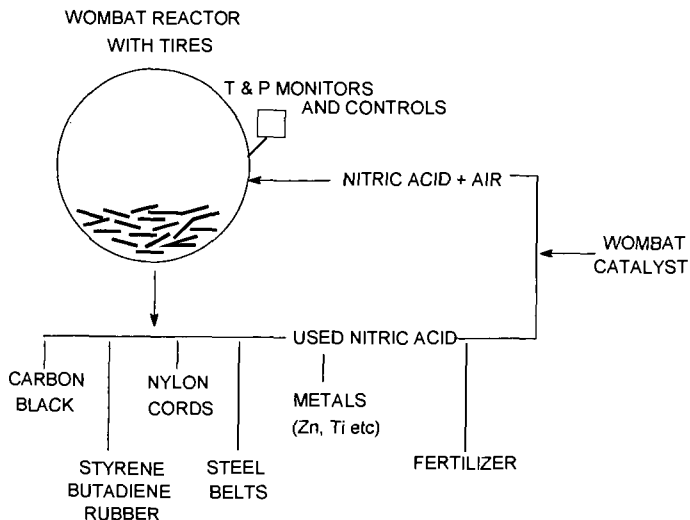


Figure 1. Schematic of new and enlarged WOMBAT reactor.

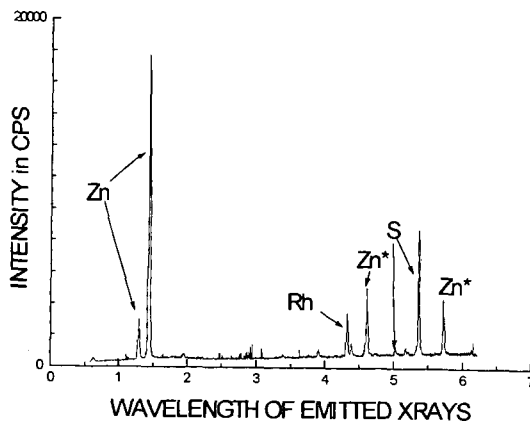


Figure 2. WDXRF spectrum of a 1" x 1" x 1/4" piece of scrap tire.

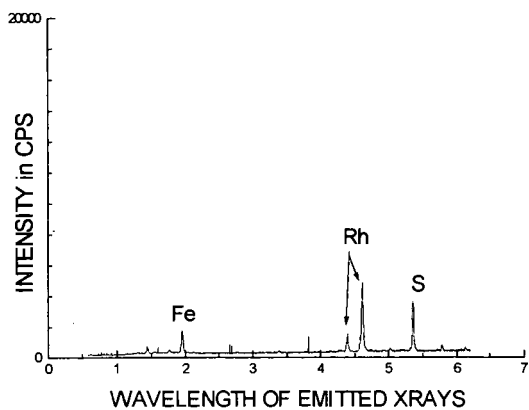


Figure 3. WDXRF spectrum of the black powder recovered from the WOMBAT reactor.

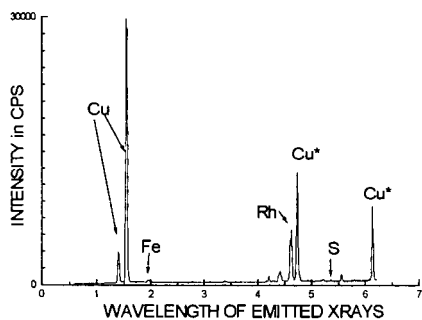


Figure 4. WDXRF spectra of the black powder prior to (circles) and after (squares) treatment with an aqueous solution containing copper(II).

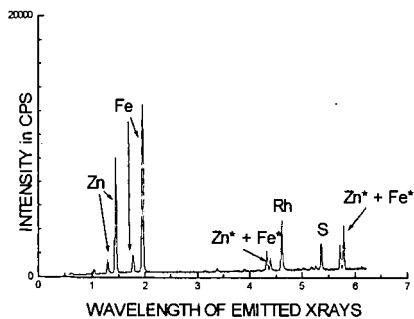


Figure 5. WDXRF spectrum of the SBR matrix recovered from the WOMBAT reactor.

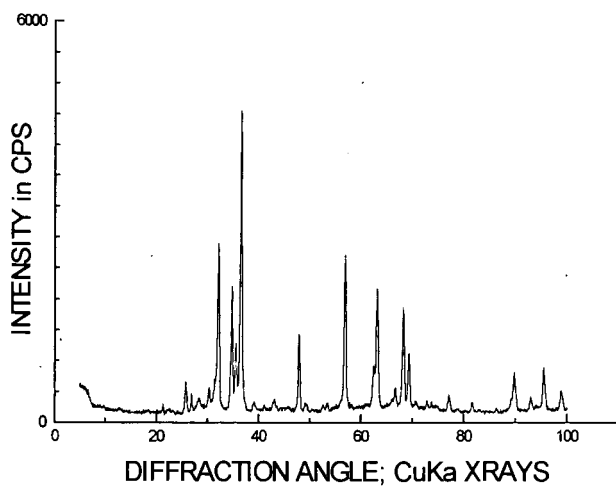


Figure 6. X-ray diffractogram of the HTA ash produced by combusting the SBR matrix.

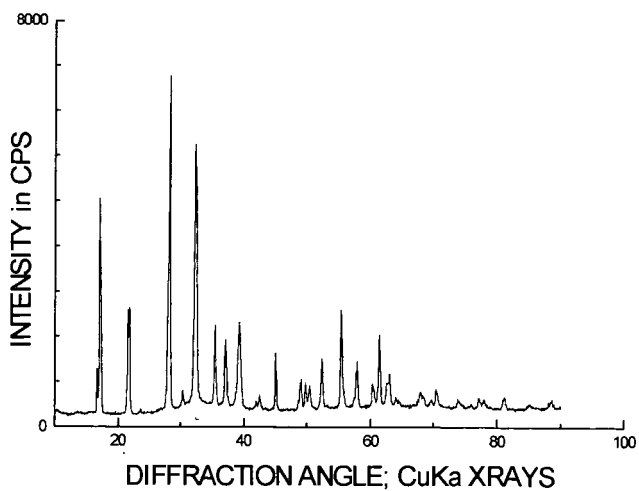


Figure 7. X-ray diffractogram of the solid produced from evaporating the mixture of "used" WOMBAT fluid and potassium hydroxide. XRD matches JCPDF 8-452, form IV ammonium nitrate.

PREOXIDATION EFFECTS ON THE ENERGETICS OF RAPID COAL PYROLYSIS

Hyok. B. Kwon

Department of Environmental Engineering
Kyungnam University, 449 Wolyoungdong Masan, 631-701 KOREA
and

Francis J. Vastola

Department of Materials Science and Engineering
Pennsylvania State University, University Park, PA 16802, U.S.A.

Keywords: rapid coal pyrolysis, preoxidation, energetics

INTRODUCTION

Thermophysical properties such as the pyroheat, specific pyroheat, and heat of pyrolysis of coal are important energetic data in design computations relating to various coal utilization processes. Moreover, these properties of coal continuously change during pyrolysis. Therefore, knowledge of the thermophysical properties of coal under conditions of rapid heating over a wide dynamic temperature range has important implications with respect to practical usage and fundamental research of coal. The endothermic heat effects during rapid coal pyrolysis have been identified qualitatively (1, 2) and quantitatively (3-5). Of particular interest in this work is the examination of the preoxidation effects on the energetics of rapid coal pyrolysis. This interest arises from the fact that mild preoxidation inevitably occurs during handling and storage prior to practical usage. This phenomenon is known as weathering and can alter the coal's calorific value, thermoplastic properties, beneficiation, coking, liquefaction, and gasification characteristics. This mild preoxidation also influence standard tests and other experimental results, and thus has important implications with respect to fundamental research on the structure and properties of coal. The objectives of this study were to determine the preoxidation effects upon subsequent pyrolysis energetics of a subbituminous coal.

EXPERIMENTAL

Apparatus. The main components of the calorimeter are the grid reactor, electrical system, and microcomputer. The microcomputer is coupled with the reactor through a voltage regulator and a multiplexed analog/digital converter for process control and data acquisition. Details of the apparatus and procedure are given elsewhere (3). The reactor is a SS (Type 315) grid which is electrically heated by a constant voltage power supply. Heating rates were controlled by an adjustable voltage regulator powered by an acid-lead battery. The low internal resistance batteries and regulator insure constant voltage at high currents (Figure 1). The SS mesh grid and a brass bar, used as a reference resistance, make up the heating circuit. The low resistance (5.17m Ω) and large mass (50g) of the reference resistor minimize the changes in resistance from the variation in temperature due to resistive heating. Therefore, the reference resistance can be assumed to be constant during the experiment. The pyrolysis temperature, defined as the temperature at the middle of the grid, is determined from a thin (50 μ m) chromel-alumel thermocouple. For a given constant voltage the grid temperature reaches a steady state at which the resistive heat input balances losses by heat transfer. After being held at the final steady state temperature for the desired time, the sample is cooled by turning the power off.

Calibration. A number of substances (Sn, Zn, Al; Aldrich Chemical Co., 5N) undergoing phase transitions at temperatures up to 933 K were tested (Table 1). Temperature calibration was carried out with melting temperatures of standard substances. At the same time, calorimetric calibration was carried out by using the enthalpies of fusion of substances at their temperatures.

Sample Selection. Coal samples were obtained from the Penn State coal sample bank. Proximate and ultimate analyses of the coals are provided by the Penn State coal database and are presented in Table 2.

Experimental Conditions. Experimental conditions are listed below:

- | | |
|------------------------------|---|
| 1. sample size | ; 6.5 \pm 1.0 mg |
| 2. particle size | ; 100 microns (140 x 170 mesh) |
| 3. drying | ; vacuum dry overnight at 383 K
and in situ for 10 min. at 393 K |
| 4. duration of reaction | ; 20 sec |
| 5. final temperature | ; 920 \pm 20 K |
| 6. heating rate | ; 415 \pm 30 K/s at 0.2 sec |
| 7. soaking time | ; 15 sec |
| 8. data acquisition interval | ; 20 ms |
| 9. preoxidation level | ; 1, 5, 10 and 24 hrs at 400 K
with air in horizontal furnace |

Procedure. After a thermocouple was welded to a new mesh, which was folded into a "sandwich" heating element, forming a 2.5 x 12 mm strip and connected across the electrodes, the cell was evacuated, charged with nitrogen gas, and pre-fired to prevent further physical and chemical change of the mesh. During the pre-firing, the mesh expanded and annealed until it reached a steady state condition. Then, 5-10 mg of coal sample was loaded into the mesh. The particles had a uniform diameter of approximately 100 μm (140 x 170 US mesh). After the coal was loaded, the cell was charged with nitrogen gas. The coal was dried inside the reactor for 10 minutes at 393 K. Next, the coal-grid system was heated with a constant voltage pulse, then cooled via simple heat dissipation. The remaining grid-char runs were made.

Data Reduction. In order to derive the thermal properties from the raw data, it is necessary to follow the reduction procedure which is described below and graphed in Figure 2. The interpretation of each symbol is given in Table 3. Figure 1 shows the equivalent electrical circuit of the reactor. By measuring at 20 ms intervals, the two voltages e_s , e_r , and e_{tc} , the temperature of the system can be measured and the power input to the system, W_i , can be calculated versus time.

$$W_i = \frac{e_s e_r}{R_r}$$

The power loss from the system at a given temperature can be calculated by determining the convective and radiative heat loss versus temperature according to the expression

$$W_l = A(T_g - T_m) + B(T_g^4 - T_m^4)$$

The terms A and B can be obtained experimentally at the end of a char run by heating the system to a series of temperature and fitting the data to above equation using an iterative technique. A check can be made to ascertain whether the radiation coefficient, B, is physically valid or not by comparing emissivity. By being able to measure the power input to the system versus time and temperature and by being able to calculate the power loss from the system versus temperature, net power absorbed by the system versus time can be calculated. From these values the integral of heat absorbed by the system versus time can be obtained. Each run would consist of three heatings, the grid alone, the coal sample in the grid, and finally the char remaining in the grid. By being able to normalize the runs to power absorbed versus temperature, the net heat absorbed by the grid, coal, and char is obtained (Figure 2d). The subtraction of the heat absorbed by the grid from that of the coal and the char runs enables the net heat requirements for heating the coal and the char to the final temperature to be obtained. The heat of pyrolysis is arrived at by subtracting the net heat absorbed by the char from that of the coal (Figure 2e). The differential of these values is shown in Figure 2f.

Preoxidation of Coal Sample. Preoxidized coal samples were prepared corresponding with 1, 5, 10, and 24 hrs of air exposure at 400 K with a horizontal furnace. Coal samples were dried 1 hr at 400 K, with nitrogen purging before oxidation. Oxygen uptake on coal samples was monitored as the gain in weight by a Fisher TGA system. Approximately 10 mg of coal were placed in the platinum sample bucket and the system was flushed with nitrogen (flow rate of 100 cc/min) for 20 min to displace air. The sample was then heated to 400 K and held at that temperature for 1 hr for drying. The nitrogen flow was then switched to dry air and changes in sample weight were monitored in time. The results are presented in Figure 3. As illustrated, the coal samples used in this study show a very mild oxygen chemisorption of 0.7% oxygen uptake after 10 hrs of air exposure. Since there is the strong possibility that gasification takes place even at the preoxidation temperature used in this study, values obtained from this thermogravimetric method provide a lower limit for the amount of oxygen added rather than an absolute one.

Estimation of Volatile Yields. Due to the reactor design, the weighing of the resulting char was difficult; therefore, the mass of remaining char could not be measured directly. Rather, the mass was estimated using heat capacity as an indicator. The basic assumption applied is that the heat capacity of char produced from the slow heating is equal to the heat capacity of char produced from rapid heating. That is, it is assumed that the heating rate will not affect the heat capacity of the remaining char. Then the mass of the char resulting from the coal pyrolysis was calculated from the experimental heat capacity data and the volatile yield was estimated. To assess the errors associated with assumption, the heat capacity of the char produced from rapid heating was also determined on a known mass basis.

RESULTS AND DISCUSSION

The thermophysical properties measured were 1) pyroheat, ΔH_{ph} , which is the energy required to heat coal to a given temperature and is the sum of the heat of pyrolysis and heat capacity over the heating temperature interval; 2) pyroheat capacity, C_{ph} , which is the pyroheat normalized over a differential temperature interval; 3) heat of pyrolysis, ΔH_{py} , which is the thermal difference between heating coal and char to the same final temperature; and 4) pyrolysis heat capacity, C_{py} , which is the heat of pyrolysis normalized over a differential temperature interval. The experimental results are presented in Tables 4 through 6.

Pyroheat. As can be seen from Table 4, pyroheat increases as temperature increases in the temperature range from room temperature to 900 K. And the unoxidized coal was the most endothermic and that the coal with the highest degree of preoxidation was the least endothermic during the pyrolysis. The pyroheats of unoxidized PSOC 64B, subbituminous B coal and the coal exposed at 400 K for 24 hrs are 993 J/g and 756 J/g at 900 K, respectively.

Pyroheat Capacity. The pyroheat capacity of coal increases up to 650 K as the energy demanded for the pyrolyzing coal increases. Above 650 K, the endothermic effect decreases and the pyroheat capacity falls to the same value as the char (Table 5). The pyroheat capacity of the char at 900 K decreases from 1.29 J/gK to 0.98 J/gK as the level of preoxidation increases. The maximum pyroheat capacities of unoxidized coal and the coal exposed at 400 K for 24 hrs are 2.16 J/gK at 610 K and 1.62 J/gK at 640 K, respectively.

Heat of Pyrolysis. The effects of preoxidation on the apparent heat of pyrolysis are presented in Figure 4. It shows that a 20% reduction in apparent heat of pyrolysis occurs within the first 10 hrs for the preoxidized coal sample. After this time interval, the apparent heat of pyrolysis approaches asymptotic values of 25% reduction. However, the effects of preoxidation could be appreciated more realistically if one examines the effective heat of pyrolysis, which is based on the actual participating fraction. Table 8 shows that the drastic 17% reduction for the coal preoxidized for 1 hrs continuously decreased to a 58% reduction for the coal preoxidized for 24 hrs. At the mild levels of preoxidation employed in this study, the effects on energetics were drastic. For example, the thermogravimetric results show that mild preoxidation of PSOC 64B resulted in only a slight oxygen uptake. However, under the rapid heating conditions, effective heat of pyrolysis for mildly preoxidized samples are reduced 58% when compared with the corresponding effective heat of pyrolysis for the unoxidized coals. The apparent heat of pyrolysis of unoxidized coal and the coal preoxidized for 24 hrs are 316 J/g and 242 J/g, respectively. The effective heat of pyrolysis of unoxidized coal and the coal preoxidized for 24 hrs are 1086 J/g and 456 J/g, respectively (Figure 5). For the preoxidized coals, the temperature at which maximum pyrolysis occurs shifts to higher temperature. However, after the initial oxidation, the temperature at which maximum pyrolysis occurs is not changed with further oxidation.

Effects of Preoxidation. The preoxidation effects on subsequent pyrolysis behavior are summarized in Table 8. The heats of pyrolysis decrease with the level of preoxidation. However, volatile yields increase with the level of preoxidation. The estimated mass of the char decreases from 70.9% to 46.9% of its original sample mass with the level of preoxidation. In other words, volatile yields increase from 29.1% to 53.1% with the level of preoxidation. Volatile yields increase from 22.5% to 29.1% as the heating rate increase from 2 K/s to 400 K/s. The heating rate effect is enhanced with preoxidation. For example, volatile yields increase with preoxidation from 22.5% to 35.4% for a 2 K/s heating rate, while volatile yields increase from 29.1% to 53.1% for a 400 K/s heating rate (Table 9). Rapid heating generates higher pressure inside of coal very quickly due to increased rate of pyrolysis. The increased pressure differential enables the pyrolysis products to more rapidly leave the coal mass with much less chance of cracking and secondary reaction. Consequently, rapid heating increases the carbon removal efficiency of hydrogen, which results in the increased volatile yields of pyrolysis. Furthermore, preoxidation results in an activating effect on the bond breaking reaction. Therefore, the heating rate effect is enhanced by the preoxidation. The preoxidation effects on the volatile yields of pyrolysis are presented in Figure 6. The effect of preoxidation on both energetics and volatile yields of pyrolysis could be attributed to the oxygen functional groups, especially the phenolic-OH group. The phenolic-OH groups could reduce the endothermicity of the fragmentation reaction by their activating effect on bond breaking. The volatile yields increase with the heating rate. This heating rate effect is enhanced by the preoxidation due to its reducing effect on endothermicity, which results in the efficient use of a given energy. In summary, rapid heating causes more extensive fragmentation of preoxidized coal when compared with unoxidized coal. This demonstrates that the preoxidation causes a change in molecular structure and leads to the extensive fragmentation of preoxidized coal.

CONCLUSIONS

The effect of preoxidation on the subsequent rapid pyrolysis behavior is significant. Mild preoxidation reduces the endothermicity of pyrolysis drastically. The unoxidized coal is the most endothermic and the coal with the highest degree of preoxidation is the least endothermic during the pyrolysis. As a result, pyroheat, pyroheat capacity, and heat of pyrolysis decrease as the degree of preoxidation increases. The volatile yields increase with the level of preoxidation. The apparent heat of pyrolysis of unoxidized coal and coal preoxidized at 400 K with air for 24 hrs are 316 J/g and 242 J/g at 900 K, respectively. Their maximum pyroheat capacities are 0.96 J/gK at 590 K and 0.7 J/gK at 630K, respectively. The effective heat of pyrolysis of unoxidized coal and the coal preoxidized for 24 hrs are 1086 J/g and 456 J/g, respectively. The yields of volatiles for unoxidized

and preoxidized coal are 29.1% and 53.1%, respectively. However, the yields of volatiles with complementary slow heating (2 K/s) for unoxidized coal and preoxidized coal are 22.5% and 35.4%, respectively.

ACKNOWLEDGEMENTS

This study was made possible by financial support from the Coal Cooperative Program at The Pennsylvania State University. The authors thank the Penn State Coal Sample Bank and Data Base for supplying the sample and the analysis of the coal used in this study.

REFERENCES

1. Freihaut, J.D.; Zabielski, M.F.; Serry, D.J. *Prepr. Am. Chem. Soc., Div. Fuel Chem.* **1982**, 27, 89-98.
2. Morel, O.; Vastola, F.J. *Prepr. Am. Chem. Soc., Div. Fuel Chem.* **1984**, 29, 77-82.
3. Kwon, H.B., Ph.D. Thesis, Pennsylvania State University, **1987**.
4. Kwon, H.B.; Vastola, F.J. *Prepr. Am. Chem. Soc., Div. Fuel Chem.* **1993**, 38(4), 1168-1177.
5. Kwon, H.B.; Vastola, F.J. *Fuel Process. Technol.* **1995**, 44, 13-24.

Table 1. Calibration

Standard substance	Literature		Measured	
	m.p.(K)	ΔH fusion(J/g)	m.p.(K)	ΔH fusion(J/g)
Sn	505.1	60.7	496	71
			496	67
			495	70
			688	120
Zn	692.7	113.0	690	127
			691	125
			928	414
Al	933.5	396.0	920	423
			932	450

Table 2. Characteristics of coal used

PSU/DOE Ident. Number: PSOC-64B

Apparent Rank : Sub-bituminous B

Seam: Monarch, Wyoming

Mine: Big Horn

Proximate Analysis, wt. %:	As Rec'd	dry	daf
Moisture	22.1	-	-
Ash	4.6	5.9	-
Volatile Matter	33.7	43.3	46.0
Fixed Carbon	39.6	50.8	54.0
Ultimate Analysis, Wt. %:	As Rec'd*	dry	daf
C	53.0	68.1	72.3
H	4.0	5.1	5.5
N	0.8	1.0	1.1
S(total)	0.3	0.4	0.5
O(by difference)	15.2	19.5	20.7

*Excludes Moisture

Calorific value, kJ/g:

dmmc	28.1
dmmf	28.9

Table 3. Data reduction symbols

English symbols

A	Coefficient for conduction and convection
B	Coefficient for radiation
e	Voltage drop
H	Enthalpy
I	Current
R	Resistance
T	Temperature
W	Power

Subscripts

g	Grid
i	Input
l	Loss
r	Reference
s	System
rm	Room
tc	Thermocouple

Table 4. Pyroheat and Specific Pyroheat of Coal

Preoxidation Time(hr)	0		1		5		10		24	
Temperature (K)	ΔH_{ph} (J/g)	C _{ph} (J/gK)	ΔH_{ph} (J/g)	C _{ph} (J/gK)	ΔH_{ph} (J/g)	C _{ph} (J/gK)	ΔH_{ph} (J/g)	C _{ph} (J/gK)	ΔH_{ph} (J/g)	C _{ph} (J/gK)
350	47	0.73	50	0.65	40	0.65	36	0.56	37	0.55
375	71	0.93	73	0.85	62	0.81	56	0.72	57	0.71
400	99	1.14	102	1.04	89	0.97	80	0.87	78	0.86
425	132	1.33	131	1.23	118	1.11	106	1.02	104	0.99
450	171	1.52	167	1.42	148	1.25	135	1.17	133	1.11
475	213	1.70	207	1.60	182	1.39	167	1.30	166	1.23
500	260	1.85	252	1.77	219	1.51	201	1.42	199	1.33
525	311	1.98	302	1.91	261	1.62	243	1.52	232	1.42
550	365	2.07	357	2.01	306	1.71	286	1.59	273	1.50
575	428	2.13	414	2.09	352	1.78	330	1.64	317	1.55
600	483	2.16	467	2.14	401	1.81	372	1.67	355	1.60
625	533	2.16	53	2.16	450	1.81	415	1.69	396	1.62
650	594	2.13	580	2.17	499	1.79	459	1.68	439	1.62
675	648	2.06	631	2.13	543	1.73	502	1.64	480	1.58
700	699	1.95	690	2.03	585	1.63	546	1.57	522	1.50
725	749	1.81	743	1.87	629	1.50	585	1.47	564	1.39
750	797	1.68	791	1.67	669	1.36	623	1.36	598	1.27
775	835	1.55	830	1.49	698	1.21	652	1.26	623	1.15
800	862	1.44	859	1.38	724	1.11	679	1.17	646	1.07
825	894	1.36	876	1.31	744	1.05	701	1.12	667	1.02
850	926	1.32	901	1.27	765	1.02	729	1.09	689	0.99
875	959	1.30	934	1.25	796	1.01	761	1.08	723	0.98
900	993	1.29	967	1.25	827	1.01	793	1.07	756	0.97

Table 5. Pyroheat and Specific Pyroheat of Char

Preoxidation Time(hr)	0		1		5		10		24	
Temperature (K)	ΔH_{ph} (J/g)	C _{ph} (J/gK)	ΔH_{ph} (J/g)	C _{ph} (J/gK)	ΔH_{ph} (J/g)	C _{ph} (J/gK)	ΔH_{ph} (J/g)	C _{ph} (J/gK)	ΔH_{ph} (J/g)	C _{ph} (J/gK)
350	35	0.49	38	0.48	30	0.41	28	0.38	30	0.37
375	53	0.60	56	0.60	44	0.51	42	0.47	43	0.46
400	71	0.70	76	0.70	60	0.61	58	0.55	58	0.54
425	92	0.79	95	0.79	79	0.68	74	0.63	74	0.61
450	113	0.88	119	0.86	100	0.75	91	0.70	92	0.67
475	136	0.95	143	0.93	120	0.79	110	0.77	109	0.72
500	164	1.02	167	0.98	142	0.82	130	0.82	129	0.76
525	192	1.07	194	1.03	165	0.84	155	0.86	150	0.80
550	217	1.12	222	1.07	188	0.86	178	0.90	171	0.84
575	250	1.16	250	1.11	209	0.87	201	0.93	192	0.87
600	280	1.20	277	1.15	229	0.89	224	0.95	215	0.90
625	312	1.25	306	1.19	252	0.90	250	0.97	239	0.91
650	340	1.30	339	1.22	274	0.92	275	0.99	264	0.93
675	375	1.33	371	1.23	298	0.94	300	1.00	287	0.94
700	409	1.34	404	1.25	323	0.95	325	1.01	309	0.96
725	445	1.34	435	1.26	348	0.96	350	1.03	333	0.98
750	484	1.34	465	1.28	370	0.98	378	1.05	359	1.00
775	513	1.33	497	1.29	395	0.98	404	1.06	358	1.01
800	548	1.32	531	1.27	419	0.99	429	1.06	409	1.01
825	577	1.31	564	1.25	446	0.98	457	1.05	436	1.00
850	614	1.30	600	1.23	472	0.98	487	1.04	464	0.99
875	645	1.29	629	1.21	498	0.97	516	1.03	491	0.98
900	677	1.29	661	1.21	524	0.97	541	1.03	514	0.98

Table 6. Pyroheat and Specific Pyroheat of Pyrolysis										
Preoxidation Time(hr)	0		1		5		10		24	
Temperature (K)	ΔH_{ph} (J/g)	C _{ph} (J/gK)	ΔH_{ph} (J/g)	C _{ph} (J/gK)	ΔH_{ph} (J/g)	C _{ph} (J/gK)	ΔH_{ph} (J/g)	C _{ph} (J/gK)	ΔH_{ph} (J/g)	C _{ph} (J/gK)
350	11	0.21	11	0.13	9	0.21	8	0.15	7	0.15
375	17	0.30	16	0.20	17	0.27	13	0.21	14	0.21
400	27	0.40	25	0.28	28	0.33	21	0.28	19	0.27
425	40	0.50	34	0.37	38	0.40	32	0.35	28	0.34
450	57	0.61	46	0.48	47	0.48	43	0.42	40	0.41
475	76	0.71	63	0.59	61	0.56	56	0.49	55	0.47
500	95	0.80	84	0.71	76	0.65	70	0.56	68	0.54
525	118	0.88	107	0.81	95	0.75	87	0.62	81	0.59
550	147	0.93	133	0.89	118	0.82	107	0.66	102	0.63
575	177	0.96	163	0.94	142	0.88	128	0.69	124	0.66
600	202	0.96	189	0.97	170	0.91	147	0.71	139	0.69
625	220	0.92	216	0.97	197	0.91	164	0.71	155	0.70
650	253	0.86	240	0.96	224	0.88	182	0.70	175	0.70
675	273	0.77	258	0.93	245	0.82	201	0.66	192	0.66
700	290	0.65	286	0.85	262	0.72	220	0.59	212	0.58
725	303	0.52	307	0.72	281	0.59	234	0.50	230	0.48
750	312	0.39	325	0.53	298	0.44	245	0.38	239	0.35
775	322	0.27	333	0.35	302	0.29	248	0.27	237	0.22
800	313	0.16	327	0.20	304	0.17	248	0.17	236	0.12
825	316	0.08	311	0.12	297	0.09	243	0.11	230	0.05
850	312	0.03	300	0.07	291	0.05	241	0.07	224	0.02
875	313	0.01	304	0.05	298	0.04	244	0.05	231	0.00
900	316	0.00	306	0.00	303	0.00	252	0.00	242	0.00

Table 7. Estimation of Volatile Yields						
	Heating Rate of Coal Run (k/s)	Volatile Yields(%) Preoxidation Time (hrs) *				
		0	1	5	10	24
Cp, char (J/gk), orig. mass of coal	400	1.29	1.21	0.97	1.03	0.98
Cp, char (J/gk), known mass of char	0.2	1.82	1.83	1.9	1.94	2.09
	400	1.84				
Mass of Char (%) at 900 K, estimated	400	70.9	66.1	51.1	53.1	46.9
Volatile Yields (%), estimated	400	29.1	33.9	48.9	46.9	53.1
* At 400 K with air						

* At 400 K with air

Table 8. Effects of Preoxidation on Subsequent Pyrolysis Behavior (At 900 K with a 400 k/s Heating Rate)

	Preoxidation Time (hrs) *				
	0	1	5	10	24
Variation in Ap. Heat of Pyrolysis	1	0.97	0.96	0.8	0.77
Variation in Ef. Heat of Pyrolysis	1	0.83	0.57	0.49	0.42
Variation in Volatile Yields	1	1.16	1.68	1.61	1.82
Volatile Yields (%)	29.1	33.9	48.9	46.9	53.1
Apparent Heat of Pyrolysis (J/g)	316	306	303	252	242
pyroheat of Char (J/g)	677	661	524	541	514
Pyroheat of Coal (J/g)	993	967	827	793	756
Effective Heat of Pyrolysis (J/g)	1086	903	620	537	456

* At 400 K with air

Table 9. Effects of Heating Rate on Volatile Yields

Heating Rate of Coal Run (k/s)	Volatile Yields (%) preoxidation Time (hrs) *				
	0	1	5	10	24
0.2	36.5	36.8	36.1	35.9	35.9
2	22.5			26.8	35.4
400	29.1	33.9	48.9	46.9	53.1

* At 400 K with air

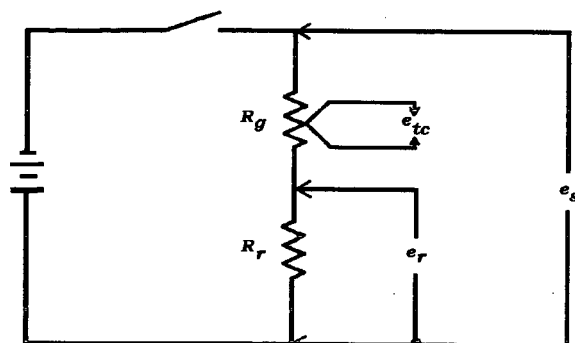


Fig. 1. Equivalent circuit of the heating system

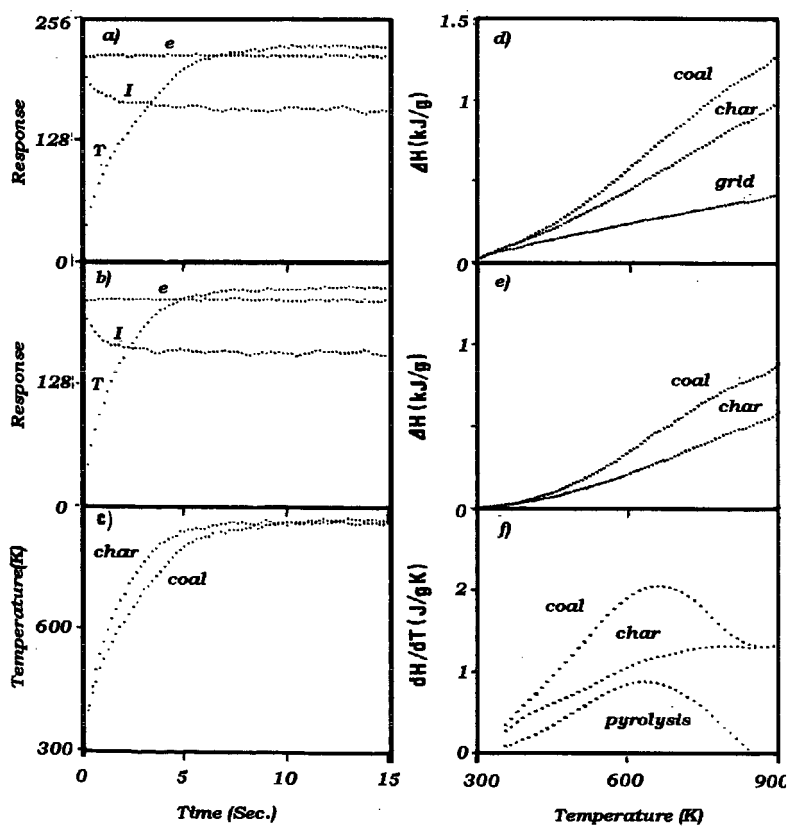


Fig. 2. Data reduction: Coal run (a), char run (b), temperature profile (c), enthalpy change (d), normalized enthalpy change (e), and rate of enthalpy change (f).

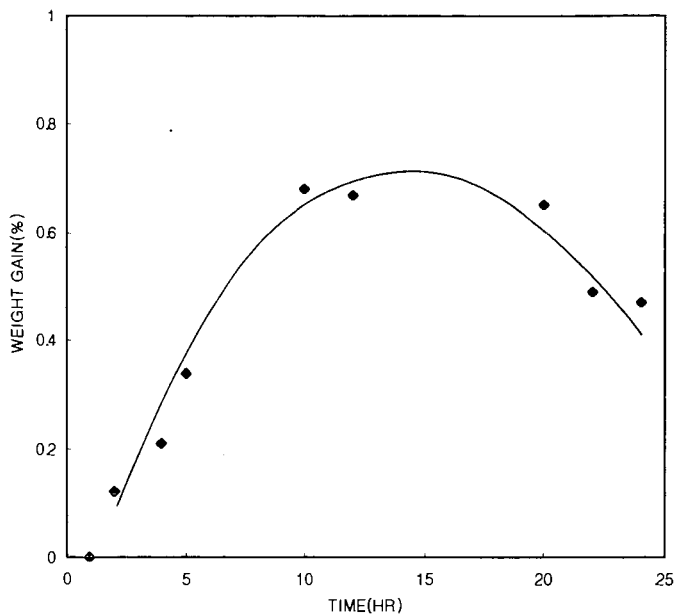


Fig 3. Weight Gain vs. Preoxidation Time

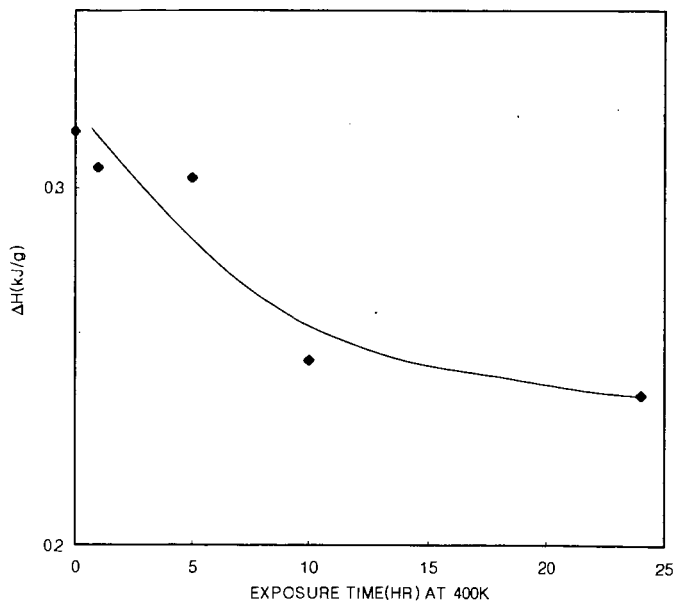


Figure 4. Apparent Heat of Pyrolysis (at 900 K)
vs. Preoxidation Time

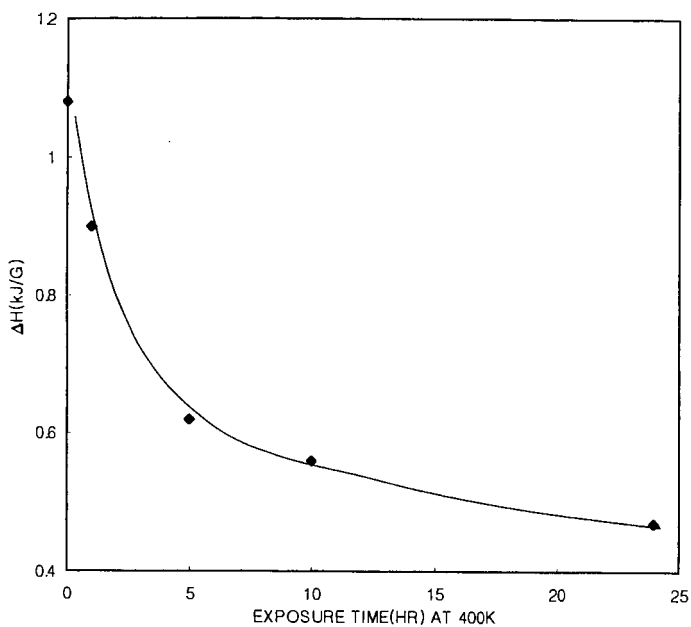


Figure 5. Effective Heat of Pyrolysis (at 900 K) vs. Preoxidation Time

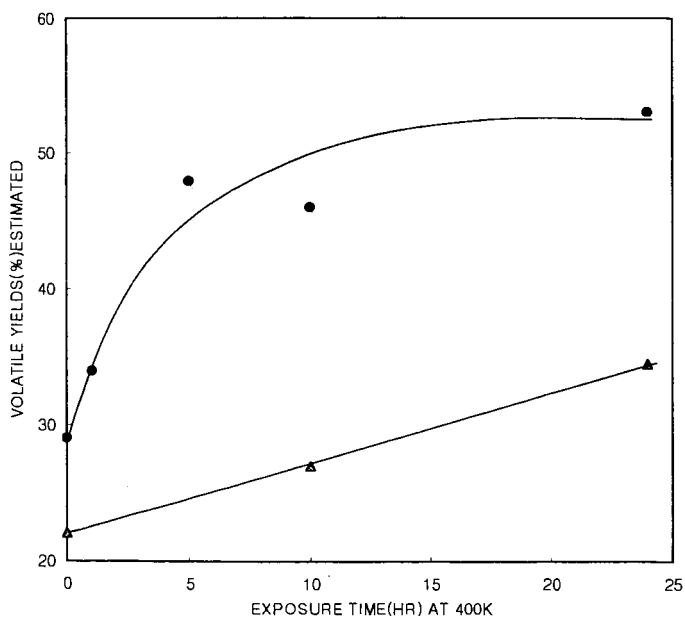


Figure 6. Volatile yields of pyrolysis (at 900 K) vs. Preoxidation Time for Different Heating Rates Heating Rate (K/s); 2(▲) and 400(●)

PREDICTING EFFECTIVENESS FACTOR FOR M-TH ORDER AND LANGMUIR RATE EQUATIONS IN SPHERICAL COORDINATES

Jianhui Hong, William C. Hecker, and Thomas H. Fletcher
Chemical Engineering Department, Brigham Young University, Provo, UT 84602

Keywords: effectiveness factor, Langmuir rate equation, correction function

INTRODUCTION

The effectiveness factor is widely used to account for the interaction between pore diffusion and reactions on pore walls in porous catalytic pellets and solid fuel particles. The effectiveness factor is defined as the ratio of the reaction rate actually observed to the reaction rate calculated if the surface reactant concentration persisted throughout the interior of the particle, i.e., no reactant concentration gradient within the particle. The reaction rate in a particle can therefore be conveniently expressed by its rate under surface conditions multiplied by the effectiveness factor.

The generalized steady-state equation in a spherical particle (a catalytic pellet or a solid fuel particle) may be expressed as:

$$\frac{d^2 C}{dr^2} + \frac{2}{r} \frac{dC}{dr} - \frac{r'''}{D_e} = 0 \quad (1)$$

where r''' is the intrinsic reaction rate per unit particle volume in $\text{mol}/\text{cm}^3/\text{sec}$ (as a function of C), D_e is the effective diffusivity, C is the local oxygen concentration (as a function of r), and r is the radial distance from the origin. The boundary conditions are

$$C = C_s, \text{ at } r = r_s \quad (2)$$

$$\text{and } \frac{dC}{dr} = 0, \text{ at } r = 0 \quad (3)$$

The intrinsic reaction rate r''' can be in different forms. One way to represent the intrinsic reaction rate is to use an m -th order rate equation:

$$r''' = k_m C^m \quad (4)$$

where k_m is the kinetic coefficient in $(\text{mol}/\text{cm}^3)^{1-m} \text{sec}^{-1}$, and m is the intrinsic reaction order. Another way is to use a Langmuir rate equation

$$r''' = \frac{k_1 C}{1 + KC} = \frac{k_0 KC}{1 + KC} \quad (5)$$

where k_1 and K are two kinetic parameters (the physical meanings of these two parameters depend on the mechanism leading to this rate equation), and k_0 is the ratio of k_1 to K . Note that the product of K and C is dimensionless.

The exact analytical solutions for the radial oxygen concentration profile and the effectiveness factor have been well established when the intrinsic reaction rate is first order.¹⁻³ Assuming that D_e is constant throughout the particle, the exact analytical solution for the effectiveness factor for a first order reaction is

$$\eta = \frac{1}{M_T} \left(\frac{1}{\tanh(3M_T)} - \frac{1}{3M_T} \right) \quad (6)$$

$$M_T = \frac{r_s}{3} \sqrt{\frac{k}{D_e}} \quad (7)$$

where r_s is the radius of the particle, k is the kinetic coefficient in $1/\text{sec}$, and M_T is the Thiele modulus. Eq. 6 is referred to in this paper as the first order curve.

Bischoff⁴ developed (in Cartesian coordinates) a general modulus for an arbitrary reaction rate form:

$$M_T = \frac{L r'''(C)}{\sqrt{2}} \left[\int_0^C D(t) r'''(t) dt \right]^{-\frac{1}{2}} \quad (8)$$

where L is the characteristic length of the particle (defined as the volume of the particle/external surface of the particle), t is a dummy integration variable, r''' is the intrinsic reaction rate per particle volume in any form, and D is the effective diffusivity, which can be a function of oxygen concentration, but is assumed to be constant in this study for simplicity. The use of this general modulus in Cartesian coordinates brought all of the curves for various m -th order rate equations and the Langmuir rate equation with different values of K into a relatively narrow band (see Figure 1). In particular, the general modulus for m -th order rate equations was derived from Eq. 8:

$$M_T = L \sqrt{\frac{(m+1) k_m C_s^{m-1}}{2 D_e}} \quad (9)$$

For the Langmuir rate equation in Eq. 5, a general modulus can be derived from Eq. 8:

$$M_T = L \sqrt{\frac{k_1}{2 D_e} \frac{K C_s}{1 + K C_s} [K C_s - \ln(1 + K C_s)]^{\frac{1}{2}}} \quad (10)$$

If accuracy is not a major concern, all of the η vs. M_T curves in the narrow band can be approximated by the first order curve, as shown in Figure 1. The method of approximating the η vs. M_T curve of a non-first order reaction by the first order curve is referred to in this paper as the first order approximation. The first order approximation method becomes more and more accurate as M_T approaches zero and infinity. However, in the intermediate range of M_T ($0.2 < M_T < 5$), the first order approximation method leads to up to -34% error in Cartesian coordinates, as shown in Figure 1. Note that in Cartesian coordinates the first order curve is

$$\eta = \frac{\tanh(M_T)}{M_T} \quad (11)$$

while in spherical coordinates the first order curve is Eq. 6.

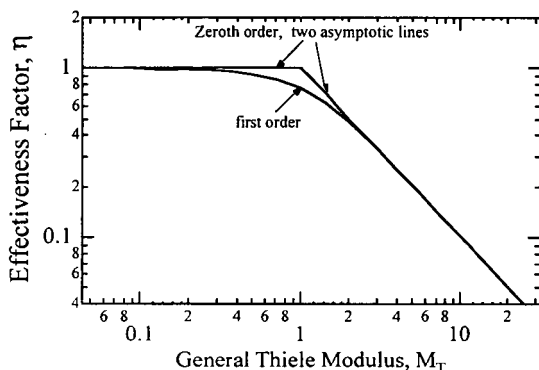


Figure 1. The effectiveness factor curves for first order and zeroth order reactions in Cartesian Coordinates. For reactions between zeroth order and first order extremes ($0 < m < 1$ or $0 < K C_s < \infty$), the curves lie in the narrow band bounded by the first order and the zeroth order curves.

RESULTS AND DISCUSSION

The Effective Reaction Order for An Arbitrary Reaction Rate Form

From the intrinsic m -th order rate equation (Eq. 4), it is easy to get

$$\ln(r''') = \ln(k_m C^m) = \ln(k_m) + m \ln(C) \quad (12)$$

From the above equation, it can be seen that if we plot $\ln(r''')$ vs. $\ln(C)$, we get a straight line, and the slope of this line is the reaction order m . Eq. 11 can be re-written as:

$$m = \frac{d \ln[r''(C)]}{d \ln(C)} \quad (13)$$

For a reaction described by a Langmuir-Hinshelwood rate equation, there is no reaction order in an explicit sense. However, the right-hand side of Eq. 12 can be used as the definition of an **effective reaction order** m_{eff} for an arbitrary reaction rate form.

$$m_{eff} = \frac{d \ln[r''(C)]}{d \ln(C)} \quad (14)$$

We now apply this definition to the Langmuir rate equation. Substitution of the Langmuir rate equation into Eq. 14 gives

$$m_{eff} = \frac{d \ln\left(\frac{k_1 C}{1 + K C}\right)}{d \ln(C)} = \frac{1}{1 + K C} \quad (15)$$

Note that for a Langmuir type reaction the $\ln(r''')$ vs. $\ln(C)$ curve is not a straight line. The slope of the curve (which is m_{eff}) is dependent on the local oxygen concentration. At the surface oxygen concentration C_s , the effective reaction order is

$$m_{eff,s} = \frac{1}{1 + KC_s} \quad \text{for the Langmuir rate equation} \quad (16.L)$$

Note that for an m -th order rate equation, the effective reaction order is always equal to m . Therefore,

$$m_{eff,s} = m \quad \text{for an } m\text{-th order rate equation} \quad (16.m)$$

Evaluation of the First Order Approximation in Spherical Coordinates

Since catalytic pellets and porous solid fuel particles can be approximated more or less by spheres, rather than by semi-infinite flat-slabs, it is of more interest to study the performance of the first order approximation method in spherical coordinates. The values of the effectiveness factor predicted by the first order curve (Eq. 6) using the general moduli in Eqs. 9 and 10 were compared to the numerical solutions. It was found that in spherical coordinates, the first order approximation method predicted the effectiveness factor more accurately than in Cartesian coordinates, with errors ranging from -17% to 0% (see Table 1). In other words, all of the curves for various values of $m_{eff,s}$ were brought into a narrower band in spherical coordinates than the band in Cartesian coordinates (see Figures 1 and 2). From Table 1, it can be seen that: 1) as the value of M_T gets away from 0.707 in both directions, the error diminishes rapidly to zero; 2) as $m_{eff,s}$ decreases from unity to zero, the error increases from zero to -17%.

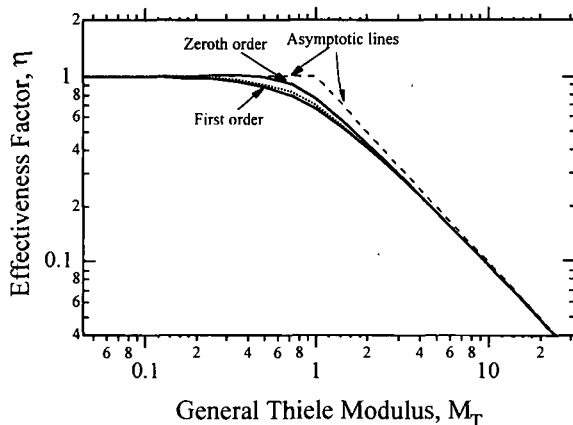


Figure 2. Effectiveness factor curves for first order and zeroth order reactions in spherical coordinates. For reactions described by the Langmuir and m -th order rate equations, the curves lie in the narrow band bounded by the first order and zeroth order curves. The dotted line in the band corresponds to $m = 0.5$ and corresponds approximately to $KC_s = 1$ ($m_{eff,s} = 0.5$ for both m -th order and Langmuir rate equations).

Table 1. The Errors (%) of the First Order Approximation Method Using the Modulus in Eq. 10

$m_{eff,s} \backslash M_T$	1.00	0.75	0.50	0.25	0.00
0.125	-0.019	-0.162	-0.342	-0.583	-0.925
0.25	-0.016	-0.588	-1.282	-2.188	-3.560
0.5	-0.013	-1.639	-3.672	-6.557	-12.375
0.707	-0.076	-2.162	-4.802	-8.618	-16.081
1	-0.215	-2.274	-4.756	-8.000	-12.392
2	-0.491	-1.584	-2.813	-4.277	-6.018
4	-0.679	-1.191	-1.774	-2.472	-3.156
8	-0.933	-1.186	-1.473	-1.821	-2.274

Note: The errors of the first order approximation method using the general Thiele modulus in Eq. 9 are almost identical to the values in this table.

Correction Function

It has been shown that in the intermediate range of M_T ($0.2 < M_T < 5$), the first order approximation method leads to up to -17% error. It is desirable to reduce the error using a multiplier with the first order curve (Eq. 6). Two correction functions were constructed to counter the errors associated with the first order approximation methods for m-th order rate equations and the Langmuir rate equation, respectively. By using the effective reaction order evaluated at the external surface oxygen concentration, these two correction functions can be unified into

$$f(M_T, m_{\text{eff},s}) = \left(1 + \frac{\sqrt{1/2}}{\frac{1}{2M_T^2} + 2M_T^2}\right)^{\frac{1}{2}(1-m_{\text{eff},s})^2} \quad (17)$$

where $m_{\text{eff},s} = m$ for m-th order rate equations, and
 $m_{\text{eff},s} = 1/(1+KC_s)$ for Langmuir rate equations.

The correction function is used as a multiplier before the right-hand-side of Eq. 6:

$$\eta = f \frac{1}{M_T} \left(\frac{1}{\tanh(3M_T)} - \frac{1}{3M_T} \right) \quad (18)$$

Note that this correction function is designed only for correcting the first order approximation in spherical coordinates, but not in Cartesian coordinates.

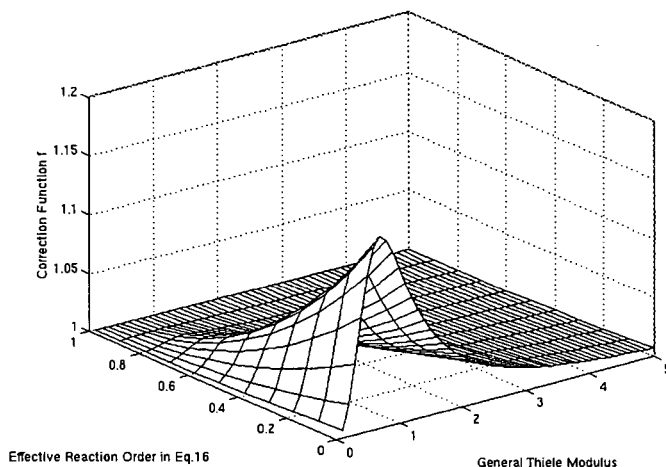


Figure 3. The correction function f vs. Thiele modulus M_T and the effective reaction order at external surface $m_{\text{eff},s}$.

Accuracy of the corrected first order approximation

Compared to numerical solutions, the corrected first order approximation predicts the effectiveness factor within 3.0% errors (see Table 2). After the effectiveness factor is obtained, the overall reaction rate in a spherical particle can be easily calculated using

$$r'''_{\text{obs}} = \eta k_m C_s^m \quad (19)$$

for a m-th order type reaction, and

$$r'''_{\text{obs}} = \eta \frac{k_1 C_s}{1 + KC_s} \quad (20)$$

for a reaction described by the Langmuir rate equation.

CONCLUSIONS

Two correction functions were constructed to improve the accuracy of predicting the effectiveness factor for the Langmuir and m-th order rate equations, respectively. By using the

intrinsic effective reaction order evaluated at surface concentration, these two correction functions were unified (see Eq. 17).

The first order curve combined with the correction function developed in this study was able to predict the effectiveness factor for m -th order rate equations and the Langmuir rate equation within 3% in the whole range of M_T (including Zone I, Zone II and especially the transition zone). This "corrected first order approximation method" uses explicit analytical expressions to predict the effectiveness factor, and therefore is particularly suitable for repeated use in comprehensive computer codes.

Table 2. The Errors of the Corrected First Order Approximation Method Using the Proposed Modulus in Eq. 10

$M_T \backslash m_{eff,s}$	1.00	0.75	0.50	0.25	0.00
0.125	-0.019	-0.030	0.163	0.485	1.133
0.25	-0.016	-0.158	0.375	1.354	0.001
0.5	-0.013	-0.729	-0.113	1.208	1.394
0.707	-0.076	-1.161	-0.849	0.128	-1.246
1	-0.215	-1.387	-1.197	0.076	1.374
2	-0.491	-1.178	-1.136	-0.324	0.545
4	-0.679	-1.068	-1.256	-1.243	-1.144
8	-0.933	-1.153	-1.337	-1.494	-1.743

Note: The errors of the corrected first order approximation method using the general Thiele modulus in Eq. 9 are almost identical to the values in this table.

ACKNOWLEDGEMENTS

This study is supported by the Advanced Combustion and Energy Research Center (ACERC) at Brigham Young University, Provo, Utah 84602.

REFERENCES

1. Aris, R., *Chem. Eng. Sci.*, **6**, 262 (1957).
2. Thiele, E. W., "Relation between Catalytic Activity and Size of Particle", *Ind. Eng. Chem.*, **31**, 916 (1939).
3. Smith, J. M., *Chemical Engineering Kinetics*, McGraw Hill, New York (1981).
4. Bischoff, K. B., "Effectiveness Factor for General Reaction Rate Forms", *A.I.Ch.E.J.*, **11**, 351 (1965).

KINETICS OF HIGH PRESSURE CHAR OXIDATION

Rebekah J. Sawaya, Jared W. Allen, William C. Hecker, Thomas H. Fletcher, and
L. Douglas Smoot

Department of Chemical Engineering, Brigham Young University, Provo, Utah 84604

Keywords: char oxidation, intrinsic kinetics, high pressure, thermogravimetric analysis, intrinsic rate expression

INTRODUCTION

The intrinsic kinetics of char oxidation at atmospheric pressure have been extensively studied (1) and are fairly well agreed upon; however, kinetic data for char oxidation at elevated pressures are very limited. In addition standard kinetic models which work at low pressures apparently fail at high pressures.

Two types of kinetic models have been proposed as the rate law for high pressure char oxidation. The first, an n th order rate expression in the form of $r = A \exp(-E_a/RT) C_{O_2}^n$ where C_{O_2} is the oxygen concentration at the external surface of the burning particle, was the assumed model for the work of Monson et al. (2). They obtained data in a high pressure drop tube reactor using conditions from 1400 to 2100 K, 5% to 21% O_2 and 1 to 15 atmospheres. Their data showed a significant pressure dependence on the apparent rate coefficients (A and E_a) using an assumed oxygen reaction order of $n = 0.5$. Their conclusion was that the n th order rate expression was not adequate at high pressure conditions (2). The second type of kinetic model that has been used is a Langmuir expression of the form $r_{in} = kC_{O_2}/(1 + KC_{O_2})$. Essenhigh and Mescher (3) attempted to apply this model to the data of Monson et al. by using a so-called "second effectiveness factor" and were able to predict Monson's data within a factor of two. Croiset et al. (4) performed experiments in a fixed-bed reactor from 2-10 atmospheres and 850-1200K with a bituminous coal char, and showed a decrease in pre-exponential factor with increasing pressure and a very weak total pressure effect above 6 atm. Ranish and Walker (5) studied graphite combustion and used the Langmuir model to explain changes in apparent activation energy and reaction order with changing temperature (733 to 842 K) and pressure (1 to 64 atm). Their data showed a slight decrease in oxygen order with increasing temperature.

In light of the limited high pressure kinetic data available and the conflicting conclusions resulting from the data that are available, it is clear that there is a need for extensive studies of the kinetics of char oxidation at high pressure.

The objective of this study is to determine the intrinsic (low temperature) high pressure kinetic rate expression for char oxidation over a range of char types and char preparations. Specifically, since this is still a work in progress, the objective of this paper is to report the effect of pressure on the char oxidation kinetics of Pittsburgh #8 char.

EXPERIMENTAL

Two different samples of Pittsburgh #8 char – designated P1 and P2 – were used in this study. Both were produced in a methane flat-flame burner (FFB) by devolatilizing Pittsburgh #8 coal at high heating rate (10^4 to 10^5 K/s), in 3-4% O_2 , and at peak gas temperatures of 1700-1800K. Sample P1 was produced at a FFB residence time of 65 ms and had a coal-to-char mass loss of 67% (6), while P2 was produced at a FFB residence time of 50 ms and had a coal-to-char mass loss of 58% (7).

All rate data for this study were obtained using a DMT high pressure thermogravimetric analyzer (HPTGA). The HPTGA allows for control of the total pressure, the flow rates and concentrations of the gases, and the gas temperature. Typically, for each run a 3-5mg sample was loaded into the mesh sample basket, the reaction chamber was brought to the desired temperature, pressure, and composition, and then, to start the run, the sample was lowered into the reaction chamber. A computer system recorded mass, pressure, and temperature continuously as a function of time. The slope of the mass loss curve was then determined and divided by the instantaneous mass (maf) mass to give the rate values on a "rate per gram available" basis.

Rate data were obtained for total pressures from one to 16 atm, oxygen mole fractions from 0.03 to 0.40, and temperatures from 748 K to 843 K. Activation energies were determined from standard Arrhenius plots (e.g. Figure 2), and oxygen reaction orders were determined from the slope of $\ln [P_{O_2}]$ vs. $\ln [rate]$ plots (e.g. Figure 3).

RESULTS AND DISCUSSION

Experimental runs performed at 15 different conditions using sample P1 were performed. Three runs were made at each condition; the average rates, along with the specified conditions for each run, are shown in Table 1. For each of the runs, plots of rate vs. char burnout such as those shown in Figure 1 were obtained. As can be seen, the char oxidation rate on a "per-gram-available basis" was found to be relatively constant, or independent of burnout, across a range of char burnouts from approximately 20 to 80%. A rate value representative of each run was calculated by averaging the rates at 10, 25, 50, and 75% burnout. Then, the values for each experimental condition (shown in the table) were obtained by averaging those values for the 3 runs at that condition.

The data obtained at 10% oxygen for both 1 atm and 4 atm were plotted in Arrhenius form to determine activation energy values, as shown in Figure 2. (Rate instead of rate constant was plotted on the ordinate since all data were obtained at the same P_{O_2}). As can be seen, the data at both pressures are quite linear and appear to have essentially the same slope. The calculated activation energy values of 32.7 and 33.2 kcal/mol for 1 and 4 atm, respectively, are very consistent with the literature value of 32.9 \pm 1.4 kcal/mol determined by Reade (6) for Pittsburgh # 8 char at 1 atm.

The effects of oxygen partial pressure on char oxidation rates at 1 atm, 823K and at 4 atm, 773K are shown in Figure 3. At 1 atm the data are quite linear on the log-log plot indicating that an nth order model with $n = 0.64$ is consistent with the data. At 4 atmospheres the data points exhibit a slight nonlinear behavior and it appears the reaction order may be decreasing as the partial pressure of O_2 increases. This would indicate that the nth order assumption is insufficient as the pressure increases, and that the Langmuir changing order model may be more appropriate at higher pressures. More data are needed to verify this hypothesis. Work is in progress to obtain similar data at pressures up to 64 atm.

The effect of total pressure (between one and 16 atm) on oxidation rate was determined, and the resulting data are shown in Table 2 and in Figure 4. All values were obtained for char sample P2, at a temperature of 773 K, and at an O_2 partial pressure of nominally 0.4 atm. (The data obtained at 16 atm were at an O_2 partial pressure of 0.48 atm, but were corrected to 0.40 atm assuming an O_2 order of 0.7). It can be seen from the graph that there is a definite effect of pressure on oxidation rate, independent of the partial pressure of O_2 . It appears as though rate increases as pressure increases, which would indicate further that the traditional nth order model is insufficient since it does not take into consideration the effect of total pressure.

CONCLUSIONS

The nth order model predominately used to characterize the kinetics of low pressure char oxidation is insufficient at higher pressures, and other models, such as the Langmuir model, need to be explored as possibilities for high pressure kinetic modeling. There appears to be a very definite effect of total pressure on char oxidation rate (independent of the oxygen partial pressure), as manifest by the fact that the reaction rate increased by a factor of three as the total pressure increased from one to 16 atm. The data also indicate that reaction order may be changing as oxygen partial pressure increases for higher total pressures.

REFERENCES

1. Suuberg, E.M., "Reaction Order for Low Temperature Oxidation of Carbons", 22nd Symposium (International) on Combustion; The Combustion Institute, Pittsburgh, PA, 79-87 (1988).
2. Monson, C.R., G.J. Germane, A.U. Blackham and D.L. Smoot, "Char oxidation and Elevated Pressure", Combustion and Flame, 100, 669 (1995).
3. Essenhigh, R.H. and A.M. Mescher, "Influence of pressure on the Combustion Rate of Carbon", 26th Symposium (International) on Combustion; The Combustion Institute, Pittsburgh, PA, 3085 (1996).
4. Croiset, E., C. Mallet, J.P. Rouan and J.R. Richard, "The Influence of Pressure on Char Combustion Kinetics", 26th Symposium (International) on Combustion; The Combustion Institute, Pittsburgh, PA, 3095 (1996).

5. Ranish, J.M. and P.L. Walker, "High Pressure Studies of the Carbon-Oxygen Reaction", Carbon, 31, 1, 135 (1993).
6. Reade, Walter, "An Improved Method for Predicting High-Temperature Char Oxidation Rates", M.S. Thesis, Chemical Engineering Department, Brigham Young University, Provo, UT, 1996.
7. Guo, Feng, "Kinetics and Mechanism of the Reaction of NO with Char: Effects of Coal Rank, Burnout, CaO, and Flue Gases", Ph.D. Dissertation, Chemical Engineering Department, Brigham Young University, Provo, UT, 1997.

Table 1. Test Conditions and Results* of Sample P1

P atm	T K	% O ₂	PO ₂ bar	Rate x 10 ⁴ (g/g(a)*s)	P atm	T K	% O ₂	PO ₂ bar	Rate x 10 ⁴ (g/g(a)*s)
1	823	3%	0.030	6.28	4	773	3%	0.122	5.03
1	823	5%	0.051	9.35	4	773	5%	0.203	6.82
1	823	10%	0.101	14.10	4	773	10%	0.405	15.29
1	823	20%	0.203	24.53	4	773	20%	0.811	20.55
1	823	40%	0.405	31.58	4	773	40%	1.621	27.81
1	798	10%	0.101	8.57	4	798	10%	0.405	32.14
1	773	10%	0.101	3.90	4	748	10%	0.405	6.62
					4	823	10%	0.405	56.51

*Each condition was replicated 3 times and average rates of 10%, 25%, 50%, and 75% burnout are given

Table 2. Test Conditions and Results of Sample P2

P atm	T K	% O ₂	PO ₂ bar	Rate x 10 ⁴ (g/g(a)*s)	P atm	T K	% O ₂	PO ₂ bar	Rate x 10 ⁴ (g/g(a)*s)
1	773	40%	.405	10.31	8	773	5%	0.405	24.70
1	773	40%	.405	10.53	8	773	5%	0.405	27.06
4	773	10%	.405	20.33	12	773	3.33%	0.405	24.28
4	773	10%	.405	15.93	12	773	3.33%	0.405	29.10
4	773	10%	.405	21.68	16	773	3%	0.486	31.49*
					16	773	3%	0.486	29.53*

* Rates are corrected to PO₂ = 0.4 atm assuming reaction order of n = 0.7

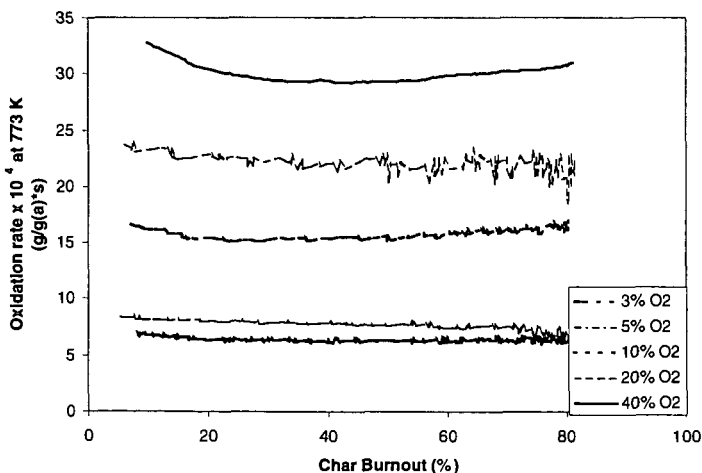


Figure 1. Effect of burnout on oxidation rate of Sample P1 at 4 atm, 773 K, and varying oxygen mole fraction.

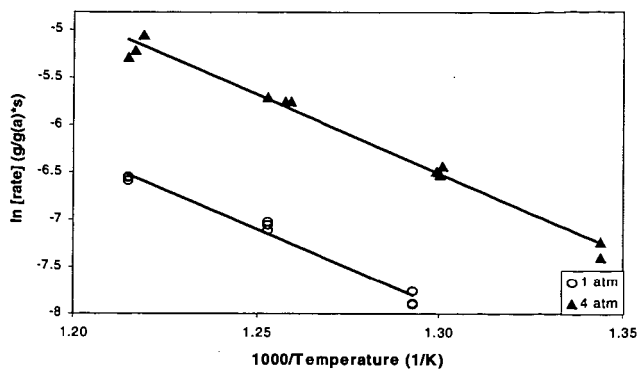


Figure 2. Arrhenius plots for oxidation rate of Sample P1 at 1 and 4 atm. All data taken at $y_{O_2} = 0.10$. Activation energies are 32.7 kcal/mol and 33.2 kcal/mol at 1 atm and 4 atm, respectively.

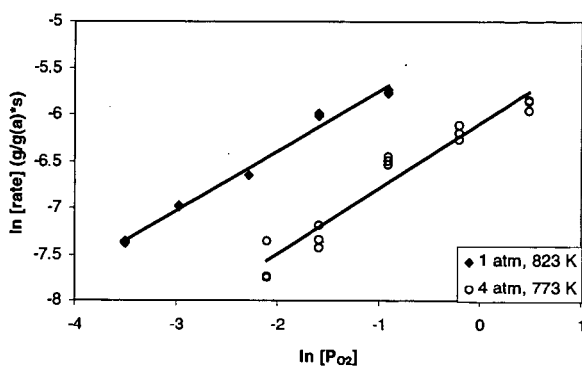


Figure 3. Effect of oxygen partial pressure on oxidation rate of Sample P1 at 1 atm (823 K) and 4 atm (773 K). Linear regression is applied to calculate reaction order using the n th-order kinetic model. Reaction orders are 0.64 and 0.70 for 1 atm and 4 atm, respectively.

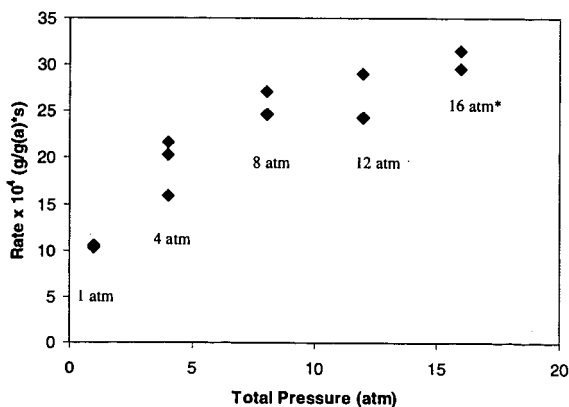


Figure 4. Effect of total pressure on oxidation rate of Sample P2 at $P_{O_2} = 0.4$ atm and 773 K. *Rates at 16 atm are corrected to $P_{O_2} = 0.4$ atm assuming reaction order of $n=0.7$.

In situ CIR-FTIR Characterization of Catalytic Cracking of Supercritical Endothermic Fuels Over Different Zeolites

Zissis A. Dardas¹, William R. Moser², Louis J. Spadaccini¹ and David R. Sobel¹

¹United Technologies Research Center

East Hartford, CT, 06108

Tel: (860) 610-7371

Fax: (860) 610-7879

E-mail: dardasz@utrc.utc.com

²Worcester Polytechnic Institute

Department of Chemical Engineering

Worcester, MA, 01609

INTRODUCTION

Endothermic hydrocarbon fuels offer the potential to be utilized as heat sinks for increased cooling for high aircraft flight speeds by undergoing cracking reactions on a zeolite catalytic substrate prior to injection into the combustion system (1, 2). For maintaining high catalytic activities over the required fuel processing times, it is necessary to minimize the amount of coke that is rapidly formed on the catalyst as a by-product in these reactions. Early studies on different hydrocarbon catalytic processes under supercritical conditions including paraffin and olefin isomerization (3-7), xylene isomerization on Ga-containing molecular sieves (8), benzene and ethyl benzene disproportionation over USHY (9), isoparaffin-olefin alkylation over MCM materials (10) and Fisher-Tropsch synthesis on silica supported metal based catalysts (11) demonstrated the beneficial effect of supercritical reaction conditions on the catalyst activity. Product selectivity differences were also observed by comparing gas phase with supercritical processes. However, all these processes were performed at temperatures only slightly above the critical temperature of the system ($1 < T/T_c < 1.1$) where significant changes in the fluid density occur with changes of the pressure near the critical pressure (12). Therefore, the observed differences were attributed to gas-like diffusivities and liquid-like densities of the supercritical fluid. The liquid-like density of the supercritical fluid should result to the in situ extraction of the coke precursors from the catalyst pores.

Sobel et al. (2) demonstrated that high temperature cracking of endothermic jet fuels at supercritical pressures ($1 < P/P_c < 4$) over zeolites resulted in an increase of the catalyst life time relative to gas phase process conditions. This was surprising since at the high temperatures required for catalytic cracking of hydrocarbon fuels (well above 450 °C), very high pressures (above 2500 psi, i.e. $P/P_c > 8$) are demanded for the supercritical fuel to reach liquid-like densities. However, the development of high temperature, high pressure packed bed autogeneous infrared monitoring microreactors for heterogeneous catalysis based on Cylindrical Internal Reflectance (CIR) revealed for the first time that hydrocarbons exposed to micropores under supercritical catalytic cracking conditions led to super dense liquid like phase within the fine pore structure (13, 14). The super dense phase observed had the effect of maintaining the activity of zeolites under high conversion cracking conditions by solubilizing in situ coke precursor molecules, resulting in lower amounts of coke deposited within the zeolitic micropores.

EXPERIMENTAL

In situ infrared spectra were acquired using a Cylindrical Internal Reflectance (CIR) annular packed-bed micro-reactor described elsewhere (13, 14). The principle of this technique is the following: When an IR beam is directed through a polished cylindrical crystal at an incident angle exceeding the critical angle, it undergoes a number of internal reflections at the interface with the catalyst sample and penetrates into it. The penetration depth at each point of internal reflection (usually around 1-1.5 μm) depends on the incidence angle, the radiation wavelength and the ratio of the refractive indices of the sample and the crystal while the number of total internal reflections for a specified incident angle is a function of the length and diameter of the crystal. The high-pressure CIR-micro-reactor was mounted in the sample compartment of the FTIR spectrometer. The cell was encapsulated within a heated copper-alloy block. A high-pressure metering pump and a downstream back-pressure regulator were used to control fuel circulation. Approximately 20 seconds were required for the reactor to reach steady-state conditions. The nominal residence times (contact times) were kept con-

steady-state conditions. The nominal residence times (contact times) were kept constant and equal to 1.3 sec for tests performed at different pressures by adjusting the fuel flow rates. A Sigma 2000 gas chromatograph was used for reaction-product identification and analysis. The products were analyzed by a flame ionization detector and separated by a Chrompack 10-ft x 0.125-in. column of n-octane on 80/100 mesh Poracil C.

RESULTS AND DISCUSSION

Two different aluminosilicate zeolites were evaluated in this study:

(1) Promoted Octacat, a commercial mixture of 27 wt. percent ultra-stable H-Y zeolite (Si/Al = 9), 3 wt. percent HZSM-5 (Si/Al = 25) and 70 wt. percent dilution matrix (mainly kaolinite clays).

(2) Two commercial HZSM-5's with different Si/Al ratios (Si/Al = 30 and 126).

The Y-type zeolite has large-pores (7.4 Å) and three-dimensional structure formed by rings of 12 linked tetrahedra with circular-pore openings, while the ZSM-5 is a medium-pore, three-dimensional, 10-membered-ring system of circular (5.5 Å) and elliptical (5.1 x 5.7 Å) interconnecting channels. Norpar 12 (a mixture of C₁₀ to C₁₃ normal paraffins) was selected as a surrogate jet fuel. Tests were conducted at pressures up to 1000 psia and temperatures up to 1300 F.

Promoted Octacat

The FTIR spectra of the C-H bonds during catalytic cracking of Norpar 12 at 950 F are shown in Figure 1 for subcritical (180 psia), critical (300 psia) and supercritical (600 and 950 psia) pressures. The substantial increase in the spectrum intensity with pressure suggests an increased concentration of the hydrocarbon molecules within the zeolitic micro-pores. This is illustrated more clearly in Figure 2, which compares the density measured within the zeolite pores (proportional to the IR signal) with the density determined from thermophysical properties data for hydrocarbon mixtures provided in the NIST computer program SUPERTRAPP³. (Both fuel densities are normalized to the density at the critical point.) The results suggest a super-dense or liquid-like reaction mixture within the pores of the zeolite at supercritical pressures. This behavior should be beneficial for the in situ solubilization/extraction of the coke precursors from the zeolitic micro-pores, resulting in a stabilization of the catalyst. However, very dense fuel could limit the diffusion within the zeolitic micro-pores and, therefore, lower the reaction rate. Thus, there may be an optimum supercritical pressure (i.e., reaction mixture density) at which the catalyst performance is maximized, for a specified operating temperature and flow rate. Outside the micro-pores and on the external surface of the catalyst, the fuel behaves as a gas, with no coke-precursor extraction potential. Buildup of coke on the external surface could eventually block the pore openings, restricting access into the active sites, and result in a partial deactivation of the catalyst.

The catalytic cracking of Norpar 12 on P-Octacat at 950 F for subcritical and supercritical pressures is presented in Figure 3. For each operating pressure, the catalyst activity decreased with time-on-stream for the first 100 minutes, and then reached a steady state with no further deactivation over the 4-hour test. As shown in the figure, conversion to gaseous products is low at this moderate operating temperature, which was specified as the maximum allowable for preserving the optical properties of the ZnSe crystal. The results demonstrate that, for a constant residence time, the catalyst activity increases with increasing pressure.

The CIR-FTIR technique is capable of monitoring in situ the amount of coke formed during the course of the reaction because the area under the coke infrared spectral bands is roughly proportional to the amount of coke deposited on the catalyst. In Figure 4, the area of the infrared coke bands is plotted as a function of the time-on-stream. This figure illustrates that coke builds up rapidly, until a steady state is reached at which time the rate of coke formation apparently equals the rate of solubility of the coke precursors by the supercritical fluid. After 4 hours of reaction at 950 psia, the pressure was gradually decreased and a significant increase in the intensity of the coke spectral bands was observed that was accompanied by a corresponding decrease in the concentration of active zeolitic acid sites.

HZSM-5

In general, HZSM-5 would be expected to have a lower tendency for coke formation than P-Octacat due to the structural geometry and position of the acid sites, which make it difficult to form large polynuclear hydrocarbons. As previously mentioned,

the channels are narrower than the Y-type zeolite, and there are no large internal cavities. Therefore, there is little space available within the zeolitic micro-pores for coke precursor molecules to grow. Thus, coke formation occurs predominately on the external surface. The catalytic activity of HZSM-5 depends strongly on the Si/Al ratio, which determines the concentration of acid sites within the zeolite lattice. The lower the Si/Al ratio, the higher the conversion, but also the higher the tendency for coke formation within the micro-pores. Therefore, there is an optimum Si/Al ratio.

The effect of pressure on coke formation during the catalytic cracking of Norpar 12 over P-Octacat and HZSM-5 (Si/Al = 126) at 950 F is illustrated in Figure 5. These experiments were conducted by initiating the reaction at the highest pressure and maintaining it for 4 hours, whereupon the pressures were reduced sequentially. Infrared spectra were collected after 1 hour of steady operation at each of the lower pressures. As this figure indicates, the integrated area under the coke infrared bands is always significantly lower for HZSM-5 than for P-Octacat, most likely due to the smaller pore openings which restrict the size (molecular weight) of the coke precursors that can form and engender a higher fluid density (solubility) within.

The conversion to gaseous products by HZSM-5 is compared to that by P-Octacat in Figure 6. In these tests, HZSM-5 was tested at 700 psia while P-Octacat was tested at 950 psia. Since the HZSM-5 contains the smaller pores, its performance is expected to optimize at a lower supercritical pressure than P-Octacat, because of the trade-off between coke precursor solubility and species diffusion. As shown in the figure, HZSM-5 with Si/Al = 126 can operate at 60-percent conversion to gaseous products for long reaction times, while a lower Si/Al ratio of 30 resulted in high initial conversion but rapid deactivation. In comparison, P-Octacat (which contains 3 percent HZSM-5 with Si/Al=25) can maintain only 10-percent conversion to gaseous products at this temperature.

Reaction Endotherms

The chemical heat sink (endotherm) is a function of not only conversion but also product distribution. Furthermore, many applications of interest involve operation at fuel temperatures that are considerably higher than the 950 F limit of the CIR apparatus. To determine the heat sink attainable with the two catalysts at higher temperatures, tests were conducted in a Bench-Scale Reactor Rig. The results of these tests are presented in Figure 7, and show that P-Octacat has approximately twice the cooling capacity as HZSM-5. These results imply that P-Octacat has the higher selectivity for unsaturated olefinic species, and suggest that a choice between catalysts should be made based on the requirements of the application, i.e., lifetime vs. heat sink capacity. Furthermore, the data suggest that the P-Octacat could be improved by replacing HZSM-5, Si/Al=25 with Si/Al=126, and increasing its concentration.

CONCLUSIONS

Supercritical catalytic cracking of Norpar 12 over different zeolites resulted in higher catalyst activity and lower coke deposition within the zeolitic micropores relative to the low pressure gas phase reaction conditions. In situ CIR-FTIR analysis demonstrated that this beneficial effect was due to the condensation effect of the supercritical hydrocarbon fuel within the zeolitic micropores. The liquid-like density of the fuel resulted in an in situ extraction of coke precursors, suppressing the coke deposition in the catalyst. Supercritical catalytic cracking of Norpar 12 over various HZSM-5's resulted in higher fuel conversion and lower coke deposition relative to P-Octacat (a commercial faujasite-type zeolite) but also in lower fuel endotherm (i.e. lower fuel cooling capacity). However, a ZSM-5 with a Si/Al ratio of 126 was found to be the optimum catalyst, since it maintained its activity for long operating times.

LITERATURE CITED

- (1) Spadaccini, L. J., Colket, M. B., and Manteny, P. J., Endothermic Fuels for High Speed Aircraft, Proceedings of the 1990 JANNAF Propulsion Meeting, October 1990.
- (2) Sobel, D. R., and Spadaccini, L. J., International Gas Turbine and Aeroengine Congress & Exposition, Houston, TX, June 5-8, 1995.
- (3) Tiltscher, H. W., and Schelchhorn, J., *Angew. Chemie. Int. Ed.*, 20, 892 (1981).
- (4) Tiltscher, H. W., and Schelchhorn, J., *Phys. Chem.*, 88, 897 (1984).
- (5) Tiltscher, H. W., and Hoffman, H., *Chem. Eng. Sci.*, 45, 5 (1987).
- (6) Ginosar, D. M., and Subramanian, B., *J. Catal.*, 152, 31 (1995).

- (7) Bhinde, M. V., and Hsu, C. Y., CA Patent, 2,693,373 (1992).
- (8) Amelse, J. A., and Kutz, N. A., US Patent, 5,030,788 (1991).
- (9) Manos, G., and Hoffman, H., Chem. Eng. Technol., 14, 73 (1991).
- (10) Altaf, H., WO Patent, 9,403,415 (1994).
- (11) Yokota, K., and Fujimoto, K., Ind. Eng. Chem. Res., 30, 95 (1991).
- (12) Reid, R. C., Prausnitz, J. M., and Poling, B. E., The Properties of Gases and Liquids, McGraw Hill, Inc., Fourth Edition, 36 (1987).
- (13) Dardas, Z., Suer, M. G., Ma, Y. H., and Moser, W. R., J. Catal., 159, 204 (1996).
- (14) Dardas, Z., Suer, M. G., Ma, Y. H., and Moser, W. R., J. Catal., 162, 327 (1996).

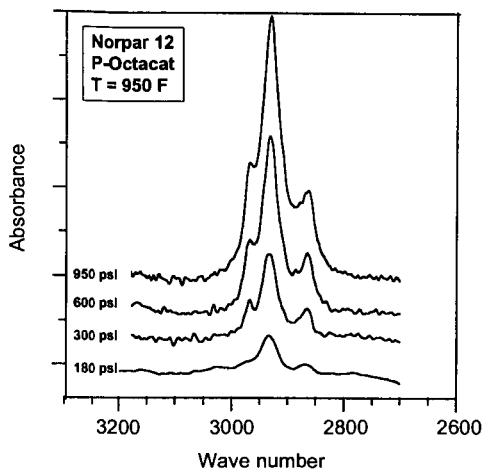


Figure 1. Infrared spectra of Norpar 12 hydrocarbon fuel C-H bonds within zeolite pores.

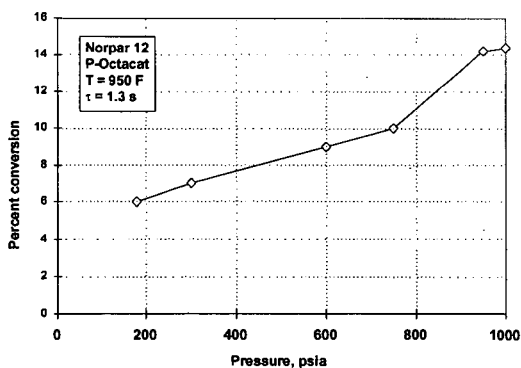


Figure 2. Reduced fuel density within zeolite pores.

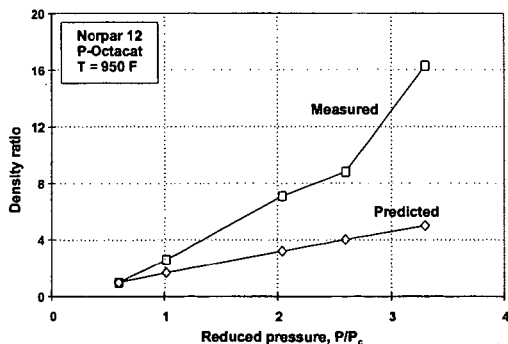


Figure 3. Conversion of Norpar 12 during catalytic cracking over P-Octacat.

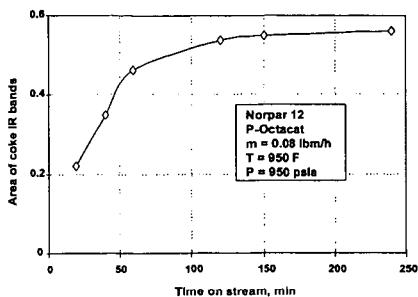


Figure 4. Area of coke infrared spectral bands.

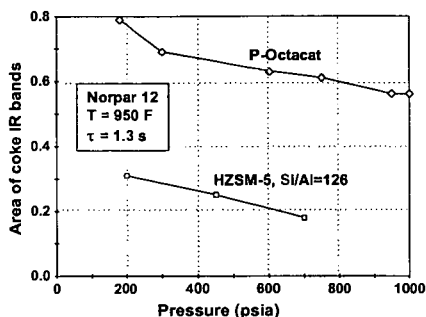


Figure 5. Effect of catalyst on coke deposition.

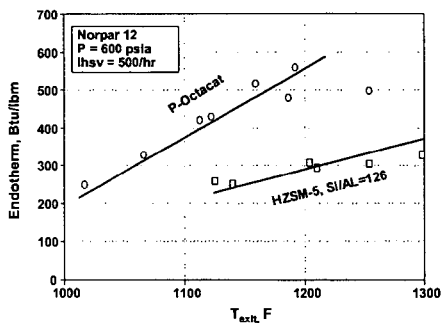


Figure 6. Degradation of catalytic activity

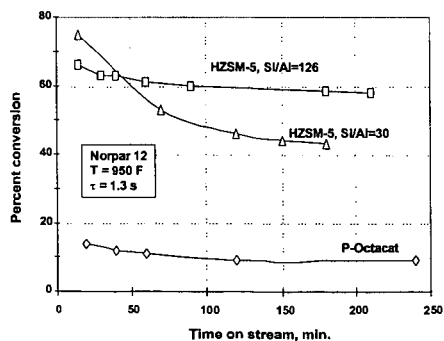


Figure 7. Endotherms for P-Octocat and ZSM-5, Si/Al=126.

FLOW PROPERTIES OF ASPHALT CEMENTS BY COMPOUNDING WITH SYNTHETIC POLYMERS

Pei-Hung Yeh, Ioan I. Negulescu and William H. Daly
Macromolecular Studies Group, Department of Chemistry,
Louisiana State University, Baton Rouge, LA 70803-1804
Louay N. Mohammad

Department of Civil Engineering and Environmental Engineering,
Louisiana State University, Baton Rouge, LA 70803

INTRODUCTION

Modification of asphalt cements with polymeric materials is widely used to improve pavement performances. Since the addition of polymers increases the cost of the corresponding polymer modified asphalt cement, industrial by-products and recycled polymers have been utilized as the modifiers within the past few years. However, understanding an asphalt-polymer system plays an important role in developing modified asphalts. This includes an understanding of the chemistry and mechanics of compatibility, reinforcement, and stability, and developing of new techniques to characterize modified asphalt binders.

Standard procedures for studying the physical and engineering properties of asphalt have been developed under auspices of the Strategic Highway Research Program (SHRP).¹ Testing and grading systems are based on measuring engineering properties that are related in a more rational way to the pavement performance. The new test methods offer the capability of measuring some properties such as rigidity, elasticity, brittleness, and durability in conditions that simulate loading and climatic conditions encountered in the field.

Our research has been devoted to characterizing asphalts and polymer modified asphalts. Polyethylene (HDPE), a recyclable waste polymer, was slightly chlorinated to improve its compatibility with asphalt.² Both HDPE and chlorinated polyethylene (CPE) modified asphalts were studied according to the Strategic Highway Research Program (SHRP) test methods to quantify the interaction of polymer with the asphalt matrix. The results of a testing protocol based upon thorough rheological evaluation of asphalts both before and after simulated aging, as well as three-point bending data at low temperature to ascertain brittleness will be reported. Preliminary characterization results on asphalt cements prepared with a CPE modified binder will be presented.

MATERIALS AND METHODS

Asphalts and Polymeric Additives

Modified asphalts were prepared using AC-10 grade materials. Polymers investigated as asphalt additives were high density polyethylene (HDPE) and chlorinated polyethylene (CPE). The properties of HDPE and CPE's (5.8 and 24.5 wt% Cl) prepared for this study were determined as previously described.³

The asphalt was heated to 150°C and stirred vigorously while either HDPE or CPE was added. Then the polymer asphalt blend was stirred at 150°C for 40 minutes.

Representative asphalts and modified asphalts were selected for thin film oven test (TFOT) and pressure aging vessel (PAV). All samples (50±0.5g) were aged in the TFOT oven @ 163°C for 5 hours under a continuous air flow. The TFOT samples were submitted to next aging step in the PAV at 100°C and 300 psi for 20 hours.

Differential Scanning Calorimetry (DSC)

Differential scanning calorimetry (DSC) data were obtained using a SEIKO DSC 220C instrument with a rate of 10°C/min. Each specimen was cooled from room temperature to -140°C, then heated from -140 to 160°C, and then was cooled from 160 to -100°C at the same rate. The glass transition temperatures (T_g), melting points (T_m), and enthalpy (ΔH) of the blend components were determined as previously described.⁴

Rheology Measurements

A dynamic shear rheometer (Bohlin CVO) was used for dynamic mechanical analysis of asphalt binders with the stress of 150 Pa @ 1.5 Hz. The samples were "sandwiched" between two parallel plates with a diameter of 25 mm at a gap of 1 mm and cooled down to 5°C through one cycle before recording measurements. The reference temperature was taken as $T = 64^{\circ}\text{C}$ to comply with the performance graded asphalt binder specification particularized for the hot climate typical of Louisiana.

Bending Beam Rheometer measurements

The bending beam rheometer (Applied Test System) was used to characterize the low temperature stiffness response of PAV aged tank asphalts and asphalt/polymer blends. The data, which were recorded at six loading times (8, 15, 30, 60, 120, and 240 sec) for a load on the beam of 100 ± 5 g, allowed the calculation of the creep stiffness, $S(t)$, and the creep rate of the sample under load, m , as the absolute value of the slope of the log creep stiffness versus log loading time curve.

Creep and Recovery Tests

A constant stress creep/creep recovery test was run at 50°C with a Haake rheometer (RheoStress RS150) using a 25 mm parallel plate system with a gap of 0.25 mm. During a first test stage, the specimen was subjected to a creep stress of 100 Pa. The resulting deformation were measured and recorded. The resiliency of the asphalt binders was evaluated after the first test phase, then the stress was released and the specimen was allowed to relax to an equilibrium deformation. The elastic recovery can be calculated by the retained deformation caused by the irreversible viscous flow process.

RESULTS AND DISCUSSION

The thermal behavior of asphalt/polymer blend is complex, and depends on asphalt sources and polymer types. Figure 1 is DSC curves of AC-10 blended with HDPE or CPE, which shows that the thermogram of AC10/HDPE blend has the melting peak (T_m) at 120°C . However, in the thermogram of AC10/CPE blend it moved down to 113°C . This phenomenon indicates that introduction of chlorine atoms onto the polymer chain can change the polymer polarity as well as the morphology by reducing the crystallinity. The resultant modification adjusts the interaction parameters to enhance dispersion of both the crystalline and amorphous regions into the asphalt phase. The T_m of CPE compounded with AC-10 decreases dramatically as the chlorine content increases. For instance, it has been observed that T_m of CPE (24.5 %wt Cl) went down to 46°C when blended with AC-10 (Figure 1).

Dynamic shear tests are advantageous because the data can be acquired in a loading mode that is similar to that of traffic loading. All isochronal $\sin\delta$ curves of blends with HDPE as illustrated in Figure 2 approached unity at higher temperatures as the viscoelastic fluids begun to flow. A $\sin\delta$ of unity confirms that the flow is Newtonian and that the polymer particles do not interfere with the measurement. However, as Figure 3 depicts, the $\sin\delta$ of blends with CPE curves are substantially less than one. Clearly, the asphalt binders containing CPE are not Newtonian even at high temperatures. The chlorinated HDPE exhibits good interaction with the polar fractions of asphalt cement which could result in increased visco-elastic properties in AC10/CPE binders and improve the pavement performance.

In Strategic Highway Research Program asphalt specifications, the stiffness parameter, $G^*/\sin\delta$, was selected to express the contribution of the asphalt binders to permanent deformations. $G^*/\sin\delta$ value should be larger than 1000 Pa @ 10 rad/s for the original binder. Higher values of the parameter ratio are expected to result in a higher resistance to permanent deformation. Isochronal plots of $G^*/\sin\delta$ (Figure 4) reveal distinct differences due to the modifiers ability to mix with asphalt. Both of the modified asphalts are qualified according to SHRP specification of the stiffness parameter at 64°C . However, only the blends containing chlorinated HDPE meet the SHRP specification at 70°C . Introduction of chlorine atoms enhances compatibility between the polymer additives and asphalt, thus the volume of the polymer rich phase is increased due to an improved 'solubility' in the asphalt. The increases are significant and are expected to result in improving pavement resistance to rutting when the pavement is open for service.

In order to evaluate the permanent deformation (rutting) and the fatigue cracking of aged asphalt binders, the SHRP specifications require determination of G^* and its components for TFOT and PAV aged materials. The permanent deformation is related to the ratio $G^*/\sin\delta$, which must be at least 2.2 KPa after TFOT aging at the specified high temperature. The product of $G^*\sin\delta$ (or G'') is represented as fatigue cracking factor in asphalt pavements, i.e. a maximum limit of 5000 KPa at a low temperature in

the SHRP asphalt specifications. The ability to dissipate or relax the stress is a desirable binder character in resisting fatigue cracking. An inspection of Figure 5 shows that there is no significant difference between tank AC10 and AC10/HDPE in the TFOT stage. Gross phase separation occurs during thin film aging of the AC10/HDPE blend, which reduces the blend properties to those of unmodified asphalt. The $G^*/\sin\delta$ of AC10/CPE blend is somewhat higher than that of the aged tank asphalt; partial phase separation occurred in this blend at high temperature but the polymer is still contributing to the blend properties. All of these binders meet the qualification of SHRP specifications at 64°C. On the other hand, tests on the fatigue cracking for PAV asphalt binders (Figure 6) show that both the loss modulus (G'') of the PAV aged AC/HDPE and of the AC/CPE blends are less than that of the PAV aged tank asphalt at all temperatures. Extrapolation of the data to the temperature at which $G^*\sin\delta$ reaches 5000 kPa illustrates this point. An estimate of the temperature for AC/HDPE or AC/CPE can be obtained from the intercept of the extrapolation which is much lower than that of the aged tank sample. It appears that a drastic reduction in the loss modulus can be attributed to the polymer additive (HDPE or CPE). This improvement should be effective in reducing age hardening and long term temperature cracking.

Preliminary low temperature creep properties of asphalt blends using a bending beam rheometer can be obtained by knowing the creep load applied to the beam and its deflection at several loading times during the test. According to SHRP program, the stiffness $S(t)$ and the creep rate of the binder under load $m = |d \log S(t) / d \log(t)|$ are reported at the specified temperature after a 60 seconds loading, which simulates the stiffness after two hours at a 10°C lower temperature. A SHRP grade temperature should meet the specifications $S(t=60) \leq 300$ MPa and m -value (slope) ≥ 0.3 . The data in Figure 7 indicate that all asphalt binders met the $S(t)$ and m -value performance criteria for the chosen temperature (-12°C).

The creep and recovery measurements provide rheological data which are characteristic to a particular binder under conditions employed. The constant stress creep/recovery test in Figure 8 illustrates a significant difference between the deformation of CPE and HDPE blends. This observation might be an indication of their rutting resistance, i.e., the lower the deformation, the better the binder response to rutting, which is related to the composition of the asphalt binder. The AC10/CPE material showed a much more pronounced resistance to creep than AC/HDPE or pure asphalt at 50°C. Elastic creep recovery of asphalt samples can be observed after the stress is removed. As expected, the AC10/CPE blend exhibited higher creep recovery than HDPE blend due to the presence of the more elastic filler. On the other hand, the pure asphalt sample did not display any recovery and the presence of HDPE in asphalt did not improve any recovery percentage under these conditions. Therefore, it would be expected to have an asphalt binder with a rutting resistance higher than the maximum resistance imparted by the tank asphalt.

ACKNOWLEDGMENTS

This work was supported by a contract from the Louisiana Transportation Research Center. Special appreciation is extended to Harold Paul who served as the contract technical representative and provided helpful and incisive comments and suggestions.

REFERENCES

1. Anderson, D., Kennedy, T.W., Proceedings of the Association of Asphalt Paving Technologists, 1994, Vol 62, 481.
2. Canterino, P.J., Kahle, G.R., J. Appl. Polym. Sci., 1962, 6, 20.
3. Daly, W. H., Negulescu, I. I., Yeh, P.-H., Prep. Symp. Am. Chem. Soc., Div. Fuel Chem., 1998, 43, 1075.
4. (a) Daly, W. H., Qiu, Z.-Y., Negulescu, I. I., Transportation Research Record, 1996, 1535, 54.
(b) Daly, W. H., Qiu (Chiu), Z.-Y., Negulescu, I. I., Transportation Research Record, 1993, 1391, 56.

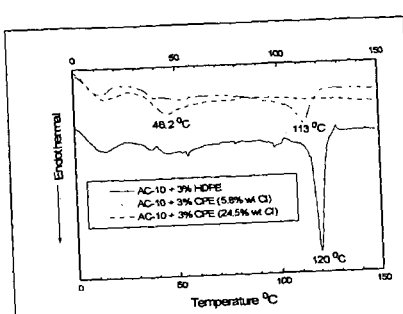


Figure1. DSC thermograms of asphalt AC-10 blended with HDPE or CPE

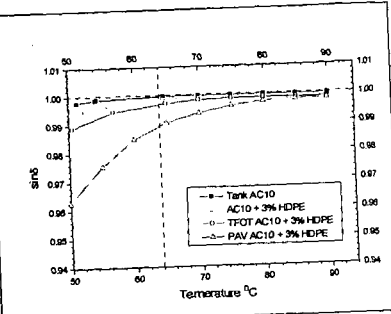


Figure2. Variation of $\sin\delta$ with temperature for a blend of AC-10 with 3% HDPE

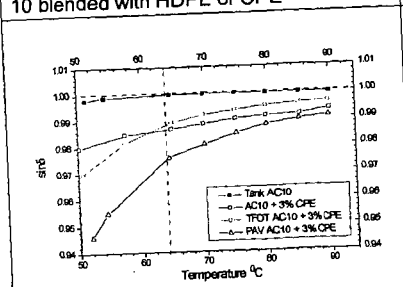


Figure3. Variation of $\sin\delta$ with temperature for a blend of AC-10 with 3% chlorinated HDPE (5.8 wt% Cl)

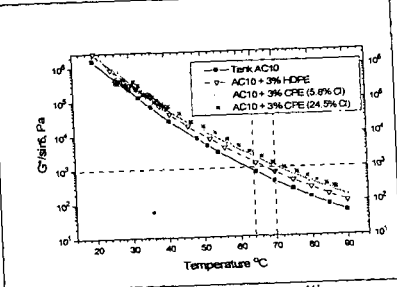


Figure4. Comparison between rutting factors of tank asphalt and blends with HDPE or chlorinated HDPE

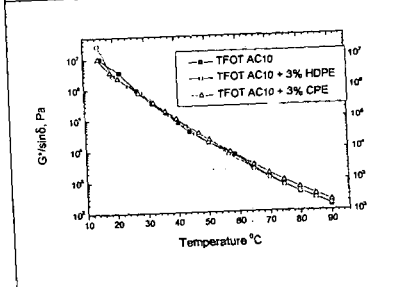


Figure5. Variation of $G^*/\sin\delta$ with temperature for tank asphalt and of blends with HDPE or chlorinated HDPE (5.8 wt% Cl)

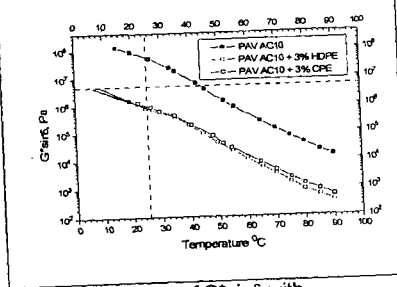


Figure6. Variation of $G^*\sin\delta$ with temperature for tank asphalt and of blends with HDPE or chlorinated HDPE (5.8 wt% Cl)

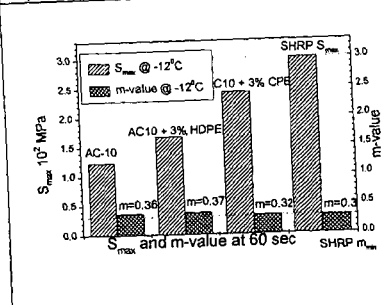


Figure7. Creep stiffness of PAV aged AC10 blends containing HDPE and chlorinated HDPE (5.8 wt% Cl)

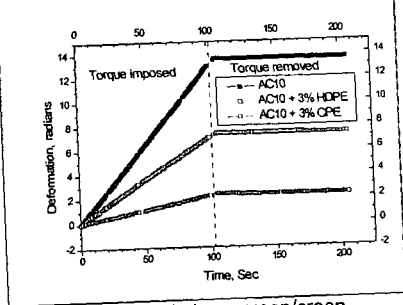


Figure8. Constant stress creep/creep recovery curves at 50 °C of AC10 blends with HDPE or CPE (5.8 wt% Cl)

Hydrogenation Reactivity of Mono-Aromatic Compound in Polar Solvents over Ru/Al₂O₃ Catalyst

Hideyuki TAKAGI, Takaaki ISODA, Katsuki KUSAKABE
and Shigeharu MOROOKA

Department of Materials Physics and Chemistry,
Graduate School of Engineering, Kyushu University,
Fukuoka 812-8581, Japan

KEY WORDS: hydrogenation, mono-aromatic compound, polarity of solvent

INTRODUCTION

Hydrogenation of aromatic compounds is a key reaction in processes such as hydrotreating of heavy oil and production of petrochemicals. Platinum group metals have the advantage of high activity for the hydrogenation of aromatic compounds under mild reaction conditions. However, the hydrogenation activity of this metal catalyst is sometimes decreased by the presence of solvents. Thus, the solvent effects can be significant, especially for the case of noble metal catalysts, which are used for the hydrogenation of asphaltene, coal extracts and polymers under mild conditions. In a previous studies [1], we reported that oxidized Yallourn coal, which had been treated with aqueous H₂O₂ in the presence of 1-propanol at 70°C, was solubilized in ethanol at a yield of 80 wt%, based on the dry raw coal mass. The ethanol-solubilized coal was further hydrogenated over a Ru catalyst at 120°C under a hydrogen pressure of 10 MPa for 72 h [2]. As a result of this catalytic hydrogenation, the aromaticity of the coal structure was altered, and the pyrolysis reactivity was increased. However, hydrogenation reactivity of aromatic compounds in solvents other than ethanol has not yet been investigated.

In the present study, therefore, benzyl alcohol was subjected to hydrogenation using Ru/Al₂O₃ catalyst at 120°C under a hydrogenation pressure of 6 MPa. Lower alcohols, non-polar solvents and solvents containing oxygen, sulfur and nitrogen were used in these reactions, and their effect on the efficiency of the reaction was examined. Carboxylic acids were also added to the reaction system, and the effect of these compounds on the hydrogenation reactivity of aromatic compounds was also determined.

EXPERIMENTAL

Chemicals and Catalysts: Benzyl alcohol was used as substrate. Methanol (MeOH), ethanol (EtOH) and 2-propanol (2-PrOH) were used for alcoholic solvents; hexane, heptane and benzene were used for non-polar solvents; acetone, 1,4-dioxane, tetrahydrofuran (THF) and diethyl ether (DEE) were used for polar solvent containing oxygen; and dimethyl sulfoxide (DMSO), N,N-dimethyl formamide (DMF) and N-methyl-2-pyrrolidone (NMP) were used for polar solvents containing sulfur and nitrogen. Formic acid (HCOOH), acetic acid (CH₃COOH), butyric acid (C₃H₇COOH) and lauric acid (C₁₁H₂₃COOH) were selected for use as added carboxylic acids in the hydrogenation reaction of benzyl alcohol. An alumina supported ruthenium catalyst (Ru/Al₂O₃, Wako chemical Co., metal content=5wt%) was used as the hydrogenation catalyst.

Reaction: The hydrogenation reactions were performed in a 50 mL batch autoclave at 120°C for 0.5 h under a hydrogen pressure of 6 MPa, equipped with a magnetic stirrer, rotating at 1000 rpm. 3 g of substrate, 6 g of solvent, and 0.5 g of catalyst were mixed, and carboxylic acid, of which usage was 3g, was further added to the reaction system. After hydrogenation, the catalyst was separated by centrifugation. Products were qualitatively and quantitatively analyzed by GC-FID (Shimadzu, GC-14A) and GC-MS (Shimadzu, QP-5000), equipped with a capillary column. The hydrogenation conversion of substrate was calculated as the following equation.

$$\text{Hydrogenation conversion [\%]} = (1 - N/100) \times 100 \quad (1)$$

where N [%] was the yield of unreacted substrate. The δ value of a solvent was defined by

$$\delta = DN - AN \quad (2)$$

where DN is the donor number, and AN is the acceptor number, of the solvent [3-4]. The relative permittivity for a mixture of solvents i and j, P_{mix} , was calculated from the following equation.

$$P_{\text{mix}} = (P_i X_i + P_j X_j) / (X_i + X_j) \quad (3)$$

where P_i and P_j are the relative permittivities of solvent i and solvent j, respectively [5]. X_i and

X_i are the mass fractions of solvent i and solvent j, respectively, ($X_i + X_j = 1$).

RESULTS

Figure 1 shows the product distributions for the hydrogenation of benzyl alcohol in the presence of the solvents. The conversion of benzyl alcohol was 76% in methanol, 82% in ethanol and 81% in acetic acid. This indicates that methanol, ethanol and acetic acid had little or no effect on the hydrogenation activity over the $\text{Ru}/\text{Al}_2\text{O}_3$ catalyst. When 2-propanol was used as the solvent, the total conversion of benzyl alcohol was decreased to 35%. When hexane and heptane, which are non-polar solvents, were used as the solvent, the hydrogenation conversion of benzyl alcohol was 75% and 61%, respectively. However, the conversion of benzyl alcohol was decreased to 35% by the addition of benzene. When acetone, THF, dioxane and diethyl ether were used as the solvent, the conversion of benzyl alcohol was 31, 36, 51 and 28%, respectively. These solvents strongly retarded the hydrogenation activity over the $\text{Ru}/\text{Al}_2\text{O}_3$. The hydrogenation of benzyl alcohol was completely inhibited when DMSO, DMF and NMP were used as the solvent.

Figure 2 shows the product distributions for the hydrogenation of benzyl alcohol dissolved in polar solvents in the presence of carboxylic acids over the $\text{Ru}/\text{Al}_2\text{O}_3$. When ethanol was used as the solvent, the hydrogenation of benzyl alcohol was increased in the presence of acetic acid, butyric acid and lauric acid. The added carboxylic acids remained unchanged during the hydrogenation reaction under the above reaction conditions. However, formic acid strongly inhibited the hydrogenation of benzyl alcohol. When THF and acetone were used as the solvent, the addition of acetic acid increased the hydrogenation reactivity, as observed in ethanol.

Figure 3 shows the pathways for the hydrogenation of benzyl alcohol over the $\text{Ru}/\text{Al}_2\text{O}_3$ catalyst at 120°C . The hydrogenation of aromatic ring (route 1) and the hydrogenolysis of hydroxy group (route 2) proceed competitively. The 1-cyclohexylmethanol is converted to cyclohexanecarbaldehyde [6]. Toluene is produced via route 2 and methylcyclohexane is produced via hydrogenation of toluene.

DISCUSSION

Figure 4 shows the relationship between the hydrogenation conversion of benzyl alcohol and the δ values of the solvents. The donor number represents the parameter which is associated with the solvent basicity, while the acceptor number is the parameter which is associated with the solvent acidity. Thus, the effect of solvents on the hydrogenation reactivity of benzyl

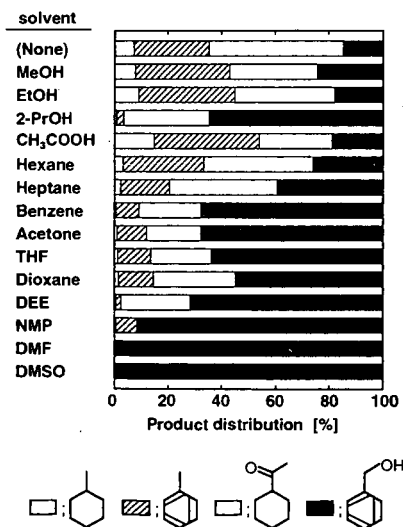


Figure 1. Product distributions for the hydrogenation of benzyl alcohol over $\text{Ru}/\text{Al}_2\text{O}_3$ catalyst.

alcohol using the Ru catalyst is classified into four categories as follows: (1) Solvents with negative δ values are capable of accepting electrons, and methanol, ethanol, acetic acid and hexane are classified into this group. The conversion with respect to the hydrogenation of benzyl alcohol is approximately 80 % for all these solvents. Thus, the negative δ values of the solvents have no effect on the hydrogenation reactivity of benzyl alcohol over the Ru catalyst. (2) Benzene and 2-PrOH possess negative δ values and accept electrons. Since benzene was hydrogenated more preferentially than benzyl alcohol, the hydrogenation of benzyl alcohol was decreased in the presence of benzene. In the case of 2-PrOH, as shown in Figure 2, the yield of toluene is decreased in the presence of 2-PrOH to a greater extent than by methanol and ethanol. Meanwhile, the yield of cyclohexanecarbaldehyde in 2-PrOH is the same as that in methanol and ethanol. Thus, the hydrogenolysis of benzyl alcohol is suppressed by the addition of 2-PrOH. (3) Solvents with positive δ values are capable of transferring electrons, and acetone, THF, dioxane and diethyl ether can be classified into this group. In the presence of these solvents, the hydrogenation conversion decreases with increasing the δ values of the solvents. Ruthenium adsorbs oxygen-containing solvents via an interaction between the surface of the ruthenium and the pair of unshared electrons of the oxygen atom of the solvents. The active sites of the catalyst are occupied by electron donor solvents to a greater extent than electron acceptor solvents, and, as the result, the hydrogenation conversion of the substrate is decreased in the presence of members of this solvent group. (4) The activity of the Ru catalyst is inactivated in the presence of DMSO, DMF and NMP, which contain either sulfur or nitrogen.

Figure 5 shows the relationship between the hydrogenation conversion of benzyl alcohol and the relative permittivity of the solutions. The relative permittivity is related to solvent polarity. The relative permittivity is 13.1 for benzyl alcohol, 24.3 for ethanol, 20.7 for acetone and 7.4 for THF. The relative permittivity of acetic acid is 6.2, which is much smaller than that of formic acid, 58.0. Thus, the polarity of mixed solvents is decreased by the addition of acetic

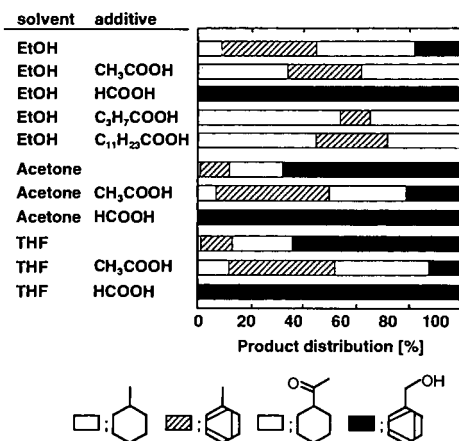


Figure 2. Product distributions for the hydrogenation of benzyl alcohol in polar solvents in the presence of carboxylic acids.

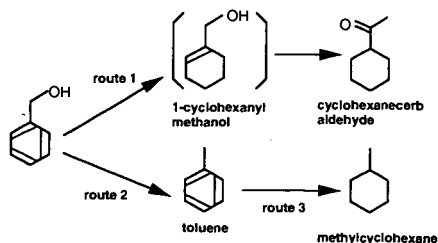


Figure 3. Pathway for the hydrogenation of benzyl alcohol over Ru/Al₂O₃ catalyst.

acid, and increased by that of formic acid. By the addition of acetic acid, the hydrogenation conversion of benzyl alcohol in ethanol, acetone and THF is increased, however, the hydrogenation reactivity is diminished by the addition of formic acid. Since formic acid is a solvent as protogenic as acetic acid, it is an electron acceptor. In addition, the relative permittivity of formic acid is much larger than that of acetic acid. Thus, the hydrogenation reactivity is affected by relative permittivity rather than the δ value for the case of formic acid.

CONCLUSIONS

1. A relationship between the hydrogenation reactivity of benzyl alcohol in polar solvent and the δ value of the solvent was found. Solvents with negative δ values did not affect the hydrogenation of benzyl alcohol over the Ru catalyst. However, solvents with positive δ values suppressed the hydrogenation of benzyl alcohol.
2. DMSO, DMF and NMP, which contained sulfur or nitrogen, deactivated the Ru catalyst.
3. The hydrogenation reactivity of benzyl alcohol in polar solvent was increased by the addition of acetic acid, butyric acid and lauric acid. The hydrogenation reactivity was related to the relative permittivity of solution. However, the hydrogenation reactivity was completely lost by the addition of formic acid with a high permittivity.

ACKNOWLEDGEMENTS

This research was supported by Japan Society for the Promotion of Science (JSPS), Organization of New Energy and Industrial Technology Development Organization (NEDO), and Center for Clean Coal Utilization, Japan (CCUJ). Support by Research for the Future Projects (Coordinator; Prof. M. Iino, Tohoku Univ.) and International Joint Research Program (Coordinator; Prof. M. Nomura, Osaka Univ.) is especially acknowledged.

REFERENCES

- [1] Isoda, T.; Tomita, H.; Kusakabe, K.; Morooka, S.; Hayashi, J.-i. *Proc. of Intern. Conference on Coal Science* **1997**, 2, 581.
- [2] Isoda, T.; Takagi, H.; Kusakabe, K.; Morooka, S. *Energy Fuels* **1998**, 12, 503.
- [3] Gutmann, V. *Angew. Chem. Internat. Ed.* **1970**, 9, 843.
- [4] Marzec, A.; Juzwa, M.; Betlej, K.; Sobkowiak, M. *Fuel Proc. Tech.* **1979**, 2, 35.
- [5] Fowler, F.W.; Katritzky, A.R.; Rutherford, R.J.D. *J. Chem. Soc. (B)* **1971**, 460.
- [6] Nishimura, S.; Hama, M.; *Bull. Chem. Soc. Jpn.* **1966**, 39, 2467.

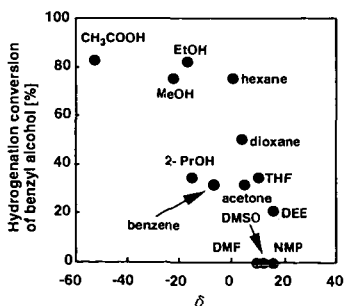


Figure 4. Relationship between hydrogenation conversion of benzyl alcohol and δ values of solvents.

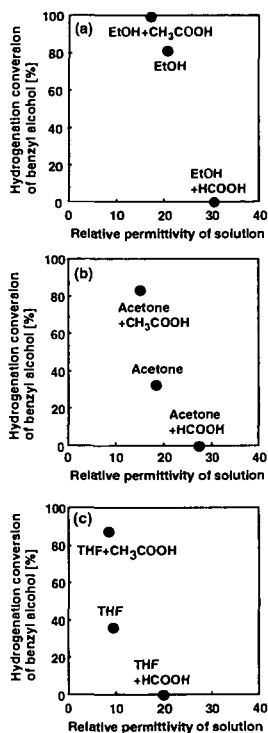


Figure 5. Relationship between hydrogenation conversion of benzyl alcohol and relative permittivity of solutions. Solvent; (a) EtOH, (b) acetone, (c) THF.

METHANE ACTIVATION AND AROMATIZATION WITHOUT USING OXIDANTS OVER Mo/H-ZSM-11 CATALYSTS

Shuang Li^a, Chunlei Zhang^b, Dongyang Wang^a, Qiubin Kan^a,
Tonghao Wu^a, Liwu Lin^b

(a. Department of Chemistry, Jilin University, Changchun, 130023;

b. State Key Laboratory for Catalysis, Dalian Institute of Chemical Physics, Chinese Academy of Sciences, PO Box 110, Dalian 116023, P. R. China)

Introduction

With the development of natural gas exploration, the catalytic conversion of methane has become one of the focal subjects of extensive research in heterogeneous catalysis. Methane aromatization without using oxidants, which produces high value and easily separated liquid aromatic hydrocarbons as well as effectively controls deep oxidation of methane, has intrigued many researchers recent years^[1-6]. As regards the supports of catalysts for this reaction, only H-ZSM-5, SiO₂, Al₂O₃ and SAPO-34 *et al* have been used up to now, and the last two have relatively low activity and selectivity^[4,5,6]. In our previous work^[7], the catalytic performance of various zeolites supported Mo-based catalysts, such as H-ZSM-11, H-ZSM-8, and H- β etc. were studied for methane non-oxidative aromatization, and possible structural rules of fine supports for this reaction were proposed. A new zeolite supported catalyst — Mo/H-ZSM-11 — was found for this reaction, which exhibits even better catalytic behavior than Mo/H-ZSM-5. In the present paper, some detailed information about Mo/H-ZSM-11 catalysts, such as the dependence of reaction temperature, space velocity of methane and MoO₃ loading on the catalytic performance of Mo/H-ZSM-11 catalysts have been studied and the optimization of the Mo/H-ZSM-11 catalyst was carried out.

Experimental

Synthesis of H-ZSM-11 zeolite and preparation of Mo/H-ZSM-11 catalysts. H-ZSM-11 (SiO₂/Al₂O₃ = 25, 50, 100, 200) was synthesized following the method in ref [8] using TBA⁺ as template by hydrothermal method.

A mixture of MoO₃ and zeolite was made by grinding. A prescribed amount of MoO₃ with the above-prepared H-ZSM-11 zeolites was thoroughly ground, then calcined at 773K for 4h in air. So the Mo/H-ZSM-11 catalyst was obtained.

Catalytic Test. Methane non-oxidative aromatization reactions were carried out in a fixed-bed continuous-flow 8-mm i.d. quartz microreactor. The catalyst charge was 1.0 g (40 ~ 60 mesh). The reaction temperature is 973K. After pretreatment, pure methane was introduced into the reactor at a space velocity of 800h⁻¹. The reaction mixture was analyzed by a on-line shimadzu GC-8A gas chromatograph in temperature programmed mode using a 3.5m Porapak P column and detected with TC detector. The methane conversion and product selectivity were calculated on a carbon number base without accounting for coking.

Results and Discussion

The effect of MoO₃ loading on the activity of Mo/H-ZSM-11 catalysts. Variations of the activity of Mo/H-ZSM-11 catalysts with different MoO₃ loadings are shown in Table 1. It can be seen that a maximum of methane conversion and benzene selectivity is observed at MoO₃ loading of 5wt%. Further increasing MoO₃ loading causes the decrease in methane conversion and aromatics selectivity notably. Therefore, the MoO₃ loading on H-ZSM-11 of about 3~5wt% is optimal, which is about the same as that on H-ZSM-5. The XRD patterns of Mo/H-ZSM-11 with different MoO₃ loadings show that the MoO₃ crystallite pattern could not be detected if the MoO₃ loading is less than 10%. It indicates that the Mo species are highly dispersed on the H-ZSM-11 zeolite in the as-prepared Mo/H-ZSM-11 catalyst.

The effect of reaction temperature on the activity of Mo/H-ZSM-11 catalysts. As shown in Fig. 1, the activity of Mo/H-ZSM-11 catalyst increases with rising temperature. It is similar to the phenomenon observed over Mo/H-ZSM-5 catalyst. This result is in correspondence with the thermodynamic calculation, that is, methane aromatization under non-oxidative condition is an endothermic reaction, therefore high temperature is more favorable to methane conversion. At different temperatures methane conversion all decrease with increasing time on stream, and the speeds of the decrease of methane conversion are in order of: 923K < 973K < 1023K < 1073K (Fig. 1), that is, the higher the reaction temperature is, the faster the methane conversion decreases. This is probably due to the increase of the carbon depositing rate over Mo/H-ZSM-11 catalysts with increasing reaction temperature. By comparison, the Mo/H-ZSM-11 catalyst shows relatively higher activity and stability at 973K, and the selectivity to aromatics is also somewhat higher. So the optimal reaction temperature on Mo/H-ZSM-11 is ~ 973K. XRD patterns of reacted catalysts at various temperatures illustrate that the structure of H-ZSM-11 zeolite is not destroyed.

The effect of methane space velocity on the catalytic performance of Mo/H-ZSM-11. The effect of space velocity of methane on the catalytic performance of Mo/H-ZSM-11 is shown in Fig. 2. Evidently, the activity of catalysts increase in order of 1500, 800, 250h⁻¹ space velocity

of methane, that is, the lower the space velocity of methane, the higher the conversion of methane, and the higher the selectivity to aromatics. Clearly, lower space velocity of methane is favorable to the conversion of methane and aromatics production. This phenomenon is similar to that obtained over the Mo/H-ZSM-5 catalyst, which indicates that on the Mo/H-ZSM-11 catalyst ethylene could also be supposed to be the intermediate of methane non-oxidative aromatization. That is, the lower the space velocity, the longer the contact time between methane and the surface of the catalyst, and the larger amount of intermediate ethylene converted to aromatics, favorable to the conversion of methane and aromatics production. This phenomenon is similar to that obtained over the Mo/H-ZSM-5 catalyst, which indicates that on the Mo/H-ZSM-11 catalyst ethylene could also be supposed to be the intermediate of methane non-oxidative aromatization. That is, the lower the space velocity, the longer the contact time between methane and the surface of the catalyst, and the larger amount of intermediate ethylene converted to aromatics.

The effect of $\text{SiO}_2/\text{Al}_2\text{O}_3$ ratio on the activity of Mo/H-ZSM-11 catalysts. The effect of $\text{SiO}_2/\text{Al}_2\text{O}_3$ ratio on the activity of Mo/H-ZSM-11 is shown in Table 2. It can be seen that with decreasing $\text{SiO}_2/\text{Al}_2\text{O}_3$ ratio, the activity of Mo/H-ZSM-11 increases. That is, the higher the $\text{SiO}_2/\text{Al}_2\text{O}_3$ ratio is, the lower the methane conversion and selectivity to aromatics are. As is well known, the lower the $\text{SiO}_2/\text{Al}_2\text{O}_3$ ratio is, the more AlO_4 tetrahedral in zeolite framework there is, as a result, the stronger the acidity of H-ZSM-11. the more AlO_4 tetrahedral in zeolite framework there is, as a result, the stronger the acidity of H-ZSM-11. Therefore, the changes of catalyst activity with different $\text{SiO}_2/\text{Al}_2\text{O}_3$ ratios reflect the effect of zeolite acidity on the reaction.

Table 1 The effect of MoO_3 loading on activity of $\text{MoO}_3/\text{H-ZSM-11}$ catalysts^a

MoO_3 loading (%)	Methane conversion (%)	Selectivity (%)		
		Aromatics (C_6+C_7)	C_2	CO
1	4.79	86.0	8.90	5.10
3	8.18	91.5	5.10	3.40
5	8.59	93.1	4.94	1.99
6	7.77	87.7	7.10	5.20
10	5.65	86.2	9.88	3.90

a. $\text{SiO}_2/\text{Al}_2\text{O}_3=25$, reaction temperature 973K.

Table 2 The effect of $\text{SiO}_2/\text{Al}_2\text{O}_3$ ratio on activity of 3%wt $\text{MoO}_3/\text{H-ZSM-11}$ catalysts at 973K

$\text{SiO}_2/\text{Al}_2\text{O}_3$ ratio	Methane Conversion (%)	Selectivity (%)		
		Aromatics (C_6+C_7)	C_2	CO
25	8.18	91.5	5.10	3.40
50	7.87	92.2	4.89	2.89
100	7.11	91.3	5.15	3.55
200	5.06	84.1	6.72	9.18

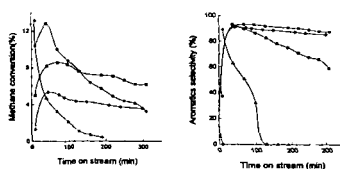


Fig.1 Methane conversion and aromatics selectivity over 5% $\text{MoO}_3/\text{H-ZSM-11}$ catalysts with time on stream at different temperatures: 923K, ♦; 973K, ■; 1023K, ●; 1073K, ▲.

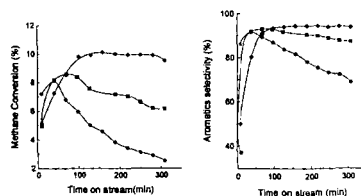


Fig.2 Methane conversion and aromatics selectivity over 5% $\text{MoO}_3/\text{H-ZSM-11}$ at different space velocity (♦, 250h⁻¹; ■, 800h⁻¹; ●, 1500h⁻¹).

References

- [1] L. Wang, L. Tai, M. Xie, G. Xu, J. Huang and Y. Xu, Catal. Lett. 21(1993)35
- [2] Y. Xu, S. Liu, L. Wang, M. Xie and X. Guo, Catal. Lett. 30(1995)135
- [3] L. Chen, L. Lin, Z. Xu, T. Zhang, and X. Li, Catal. Lett. 39(1996)169
- [4] S. Wong, Y. Xu, L. Wang, S. Liu, G. Li, M. Xie and X. Guo, Catal. Lett. 38(1996)39
- [5] F. Solymosi, A. Erdohelyi and A. Szoke, Catal. Lett. 32(1995)43
- [6] D. Wang, J. H. Lunsford and M. Rosynek, Paper presented at the 14th Meeting of the North American Catalysis Society, Snowbird, 1995;
- [7] C. Zhang, S. Li, Y. Yuan et al. Catal. Lett. 56(1998)207
- [8] G. A. Jablonski, L. B. Sand and J. A. Gard, Zeolites 6(1986)396